BOEING SCIENTIFIC RESEARCH LABORATORIES DOCUMENT D1-82-0991

BOEING

SCIENTIFIC RESEARCH LABORATORIES

Orderly Structure in Jet Turbulence

S. C. Crow

F. H. Champagne

FLIGHT SCIENCES LABORATORY

JULY 1970

99

D1-82-0991

FLIGHT SCIENCES LABORATORY

BOEING SCIENTIFIC RESEARCH LABORATORIES

ORDERLY STRUCTURE IN JET TURBULENCE

S. C. Crow

F. H. Champagne

July 1970

Table of Contents

Acknowledgment

Our research has benefited from the encouragement and occasional active participation of Earll Murman and of Steven Orszag, during his summer visit to The Boeing Company in 1969. The course of the research was influenced by stimulating discussions with several workers in the field, notably Hans Liepmann, John Ffowcs Williams, Erik Mollo-Christensen, Peter Bradshaw, and Lester Kovasznay. We owe thanks to them and to Frederick Lange, whose technical assistance expedited every phase of the program.

This paper deals chiefly with experiments on the orderly structure of jet turbulence. A mathematical study is under way and should be presented in a second paper, to be followed in due course by a third on a technological application of the phenomenon.

Abstract

Past evidence suggests that a large-scale orderly pattern may exist in the noise-producing region of a jet. Using several methods to visualize the flow of round subsonic jets, we watched the evolution of orderly flow with advancing Reynolds number. As the Reynolds number increases from order 100 to 1000, the instability of the jet evolves from a sinusoid, to a helix, and finally to a train of axisymmetric waves. At a Reynolds number around 10,000, the boundary layer of the jet is thin, and two kinds of axisymmetric structure can be discerned: surface ripples on the jet column, thoroughly studied by previous workers, and a more tenuous train of large-scale vortex puffs. The surface ripples scale on the boundary-layer thickness and shorten as the Reynolds number increases toward 100,000. The structure of the puffs, by contrast, remains much the same: they form at an average Strouhal number of about 0.3 based on frequency, exit speed, and diameter.

To isolate the large-scale pattern at Reynolds numbers around 100,000, we destroyed the surface ripples by tripping the boundary layer inside the nozzle. We imposed a periodic surging of controllable frequency and amplitude at the jet exit, and studied the response downstream by hot-wire anemometry and schlieren photography. The forcing generates a fundamental wave, whose phase velocity accords with the linear theory of temporally growing instabilities. The fundamental grows in amplitude downstream until nonlinearity generates a harmonic. The harmonic retards the growth of the fundamental, and the two attain saturation intensities

roughly independent of forcing amplitude. The saturation amplitude depends on the Strouhal number of the imposed surging and reaches a maximum at a Strouhal number of 0.30. A root-mean-square sinusoidal surging only 2% of the mean exit speed brings the preferred mode to saturation four diameters downstream from the nozzle, at which point the entrained volume flow has increased 32% over the unforced case. When forced at a Strouhal number of 0.60, the jet seems to act as a compound amplifier, forming a violent 0.30 subharmonic and suffering a large increase of spreading angle. We conclude with the conjecture that the preferred mode having a Strouhal number of 0.30 is in some sense the most dispersive wave on a jet column, the wave least capable of generating a harmonic, and therefore the wave most capable of reaching a large amplitude before saturating.

1. Introduction

We set out to find whether jet turbulence is orderly in any sense, and whether the order can be enhanced and controlled by a slight periodic surging imposed at the jet exit. The technological motivation for the study was jet noise. To the extent that turbulent mixing can be accomplished by an orderly process, a new range of noise-suppression techniques becomes available, and the problem of predicting jet noise becomes much simpler.

How does the disorder usually attributed to turbulence originate? One approach to an answer is to consider why a vorticity-free potential flow is *not* necessarily random. An incompressible potential flow is determined at each instant by conditions on the boundary. In principle, an experimentalist could establish or annihilate an incompressible potential flow instantaneously by a suitable change in the boundary conditions. He need not reach within the boundary to control the motion. Furthermore, the potential at an interior point is a weighted average of the potential over the boundary, so a local irregularity on the boundary has only a local effect inside. From instant to instant, the gross features of the boundary conditions control the gross character of an incompressible potential flow within.

The situation changes fundamentally if vorticity sheds from the boundary into the flow, as occurs continuously from a jet orifice. The flow no longer depends strictly upon instantaneous surface conditions, and the experimentalist cannot control the rotational part of the velocity

field by taking action at the boundary. *He has lost control over the flow.* The velocity at an interior point, moreover, can depend sensitively on a nearby element of vorticity and is no longer a smooth average. The flow now depends not merely on instantaneous surface conditions, but on the entire history of vortex shedding from the boundary in all detail. In order to restore control, the experimentalist must either control the three-dimensional vorticity field directly by means of body forces, or control the entire history of the boundary conditions, which is the alternative adopted in this study. Usually neither is attempted, and the flow gives way to chaos.

Despite the loss of control, the boundary conditions and mean-flow characteristics may still dispose the turbulence to acquire a somewhat orderly pattern, at least with respect to the largest scales of motion. Some classical theories of turbulent shear flow are based on that idea. Reynolds (1894) derived the original criterion for turbulence in a channel by calculating the exchange of energy between the mean flow and a train of sinusoidal eddies. Malkus (1956) based his channel-flow theory on the eigenmodes of the stability problem for the mean flow rather than an *ad hoc* sinusoidal eddy shape. The theory bearing most directly on the present work is that of Landahl (1967), who argued that the random component of boundary-layer turbulence excites relatively coherent and long-lived waves, the most lightly damped eigenmodes of the linear stability problem. The turbulence plays two roles, as a random exciter of waves, and as an ensemble of the waves themselves.

There is also a body of experimental evidence for orderly structure

in turbulent flows, even at extremely large Reynolds numbers. The Karman vortex street disintegrates at Reynolds numbers above 200,000 and was thought to be associated with moderate Reynolds numbers only. At a Reynolds number of 3,500,000, however, Roshko (1961) found that the vortex street behind a circular cylinder reappears with much the same structure as at moderate Reynolds numbers. In their flow-visualization experiments on turbulent boundary layers, Kline, Reynolds, Schraub & Runstadler (1967) discovered that turbulence production occurs in definite bursts near the wall. Presumably the bursts involve rapid stretching of vortex loops shed from the viscous sublayer. In any case, the bursts have a common structure and are random chiefly with respect to their origin in space and time.

The study of orderly jet fluctuations began during an evening of chamber music in the mid-nineteenth century. Among the audience was a medical doctor knowledgeable in acoustics, who noticed a gas flame dance in response to the violoncello so that *"a deaf man might have seen the harmony"* (Leconte 1858). The phenomenon attracted the attention of Tyndall (1867), who showed that ignition is not essential; any jet on the verge of becoming turbulent is sensitive to musical notes. The explanation of sensitive jets is due to Rayleigh (1896). The vortex sheet surrounding a jet column is unstable, so a sound wave passing the jet exit excites a train of interfacial waves on the column. The waves promote transition to turbulence and enhance mixing. Rayleigh could draw no certain conclusion about the precise shape of the waves, whether the column becomes sinuous or pulsatile, and the question has remained open since (cf. Reynolds 1962).

Questions of detail aside, it was clear by the turn of the century

that sensitivity resides in an orderly oscillation of the jet column. The nineteenth-century workers dealt with Reynolds numbers around 1000, however, and it may be wondered whether any order persists at the far greater Reynolds numbers of current technological interest. A degree of order can be inferred from casual observations of turbojet exhausts, which often appear to disintegrate into trains of loosely packed puffs of smoke. More reliable evidence is a schlieren photograph of a turbulent jet published by Bradshaw, Ferriss & Johnson (1964) and reproduced here with their kind permission as figure 1. The jet emerged with a speed of 280 ft/sec, uniform across the two-inch diameter exit plane. The corresponding Reynolds number was about 300,000 based on diameter, and the Mach number was sufficiently low that the flow can be considered incompressible. The change in refractive index was achieved by injecting Freon-12 gas into the plenum upstream of the jet. Beneath the stippled chaos of the fine mixing-layer turbulence, one can discern a train of large-scale puffs or waves.

Jet noise itself provides some evidence for natural organized structure. Mollo-Christensen (1967) observed that pressure fluctuations outside a fully turbulent jet column come in rather well defined wave packets, as though the column were undergoing sporadic oscillations. Unlike most turbulent velocity spectra, the jet-noise spectrum has a distinct peak, at a Strouhal number of about 0.3 based on frequency, exit speed, and diameter, the exact Strouhal number depending on angle from the jet axis (Mollo-Christensen, Kolpin & Martuccelli 1964). The existence of a peak suggests that an underlying wave structure may be responsible for much of the sound.

Encouraged by the available evidence, we undertook experiments on

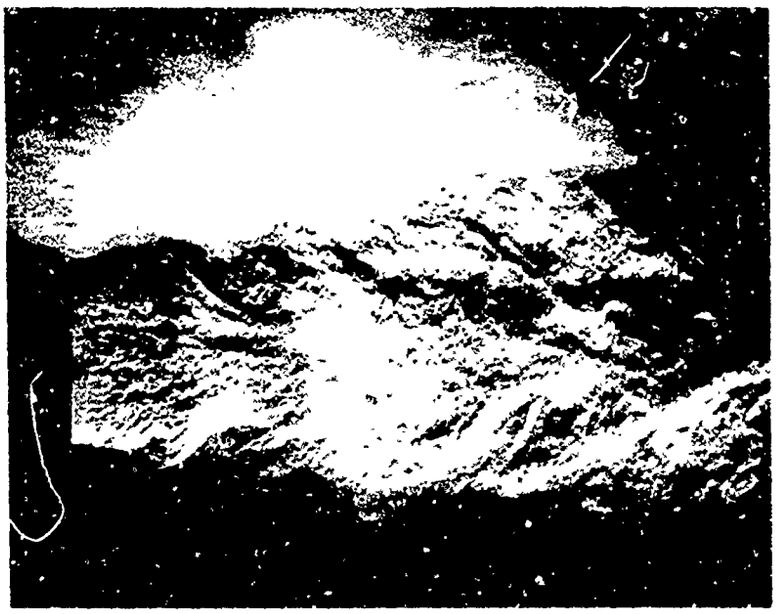

Figure 1. Gas-injection schlieren photograph of a 2-inch diameter air jet at a speed of 280 ft/sec (courtesy of Bradshaw *et al* 1964). The Reynolds number is 300,000.

round turbulent jets. The Mach number was always very small -- not so severe a restriction, because compressibility does not alter the structure of jet turbulence until the mean flow greatly exceeds the speed of sound (Ffowcs Williams 1963). We began with the flow-visualization experiments reported in §2. An orderly axisymmetric pattern was evident for Reynolds numbers between several hundred and perhaps 70,000, above which no method of visualization gave results better than those of Bradshaw *et al* (figure 1). The next step was to modify the apparatus as described in §3 so that a sinusoidal surging could be imposed at the exit plane. We thereby assumed partial control over the history of the boundary conditions in the hope of overriding the natural tendency toward chaos at high Reynolds numbers. Even when the boundary layer at the exit was tripped and fully turbulent, axisymmetric modes of organized flow could be excited and raised to high amplitude above the random background. The mode having a Strouhal number of 0.30 could attain an especially high amplitude. The structure of that preferred mode is discussed in §4, and §§5-7 explain how a nonlinear cascade establishes the Strouhal-number preference. The influence of the preferred mode on the mean field and on uncontrollable background turbulence is described in §8.

When no periodic surging is imposed, then background turbulence may trigger organized modes at random in the spirit of Landahl (1967), but the mechanism for selecting the dominant mode is different. All modes in a turbulent boundary layer are damped according to linear stability theory, so Landahl assumed that the most lightly damped mode would prevail. In the case of a round jet with a top-hat exit profile, all modes are

and the higher the frequency, the faster the amplification. But all modes saturate owing to a nonlinear cascade, and the mode having a Strouhal number of 0.30 has the highest accessible amplitude.

The relation between the orderly structure and linear stability theory is discussed in §9, and some speculations about nonlinear amplitude saturation are offered in §10, which concludes the paper. It is worthwhile laying to rest a question here, whether the phenomenon under study consists of eddies or waves (cf. Moffatt 1969). We shall move freely between both kinds of description, sometimes calling the orderly structure a vortex train, and sometimes waves on a jet column. The two descriptions are entirely complementary as far as jet turbulence is concerned. Wave terminology conveys the fact that the periodic structure obeys the dispersion relation for linearized waves on a jet column (Batchelor & Gill 1962), whereas eddy terminology emphasizes the amplitude saturation resulting from a nonlinear cascade.

2. Flow-Visualization Experiments

Viscosity influences jet turbulence primarily by affecting the boundary layer shed from the nozzle (Bradshaw 1966). The boundary layer depends on the contraction upstream of the nozzle, as well as on the Reynolds number based on exit speed and diameter. At a sufficiently low Reynolds number, however, the boundary layer of any nozzle is so thick that the exit profile resembles a Poiseuille pipe flow. We therefore began with qualitative experiments on a water jet having Poiseuille-flow exit conditions.

The jet issued from a horizontal 9-inch long glass tube submerged several inches in a large water trough. The inside diameter of the tube was 0.25 inches, and the flow rates were of order 1 ft/sec. Water for the jet was drawn from a tap and sent through a fluorescein-dye injector before entering the tube, so the jet could be seen as a bright yellow column against the black bottom of the trough. To prevent the trough filling with dye under continuous operation, a cup-shaped collector was located several inches downstream from the jet and connected to a drain. Except at the lowest flow rates, the jet appeared chaotic under normal illumination, but a stroboscope revealed the underlying order for Reynolds numbers up to about 2500, where the pipe flow itself became turbulent.

The first sign of instability was the sinuous, whiplash motion sketched in figure 2(a). The remaining parts of the figure show how the instability evolves with advancing Reynolds number. Flow rates were not measured accurately, and the drawings cannot be associated with specific Reynolds numbers. It is sufficient to note that the evolution from sinuous to pulsatile flow is complete at a Reynolds number of order 1000. As the Reynolds number advances toward that value, the sinuous column coils into a corkscrew shape (b), then tightens and forms bulbous lobes rather like a crankshaft (c), and finally breaks into a train of axisymmetric puffs (d). The helical types of instability could have either sense of revolution and would switch at random from one to the other when the tap was turned on and off. The evolution from a sinuous to a pulsatile instability was smooth and continuous, without the variety of motion seen by Reynolds (1962), whose vertical dye jet may have been slightly buoyant.

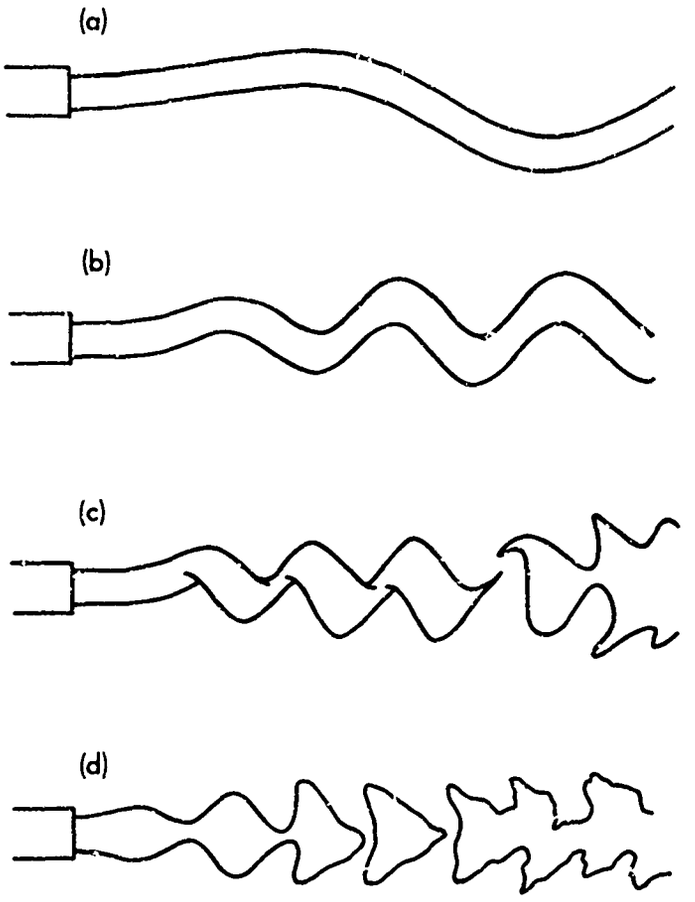

Figure 2. Evolution of jet instability with advancing Reynolds number. Parts (a)-(d) span the Reynolds-number interval from around 100 to 1000.

By moving our horizontal jet up toward the surface, we could see water waves radiating outward from above the region of puff formation. The chaotic turbulence further downstream did not appear to be a strong source of waves. Presumably because of their dispersive character, the waves were confined to narrow sectors at 45° to the jet axis. The dye jet and the synchronized waves on the surface above were beautiful under stroboscopic illumination and can be recommended as a lecture-room analogue of jet-noise production.

The Reynolds number of the dye jet could not be driven far above order 1000 before the pipe flow itself became turbulent, so we turned to the air jet shown schematically in figure 3. Not shown are an air conditioner capable of holding the jet temperature to within 1°F of the room temperature for hot-wire studies, a primary air filter, and a 1.5 hp centrifugal blower. Air from the blower enters a short diffuser S, is cleaned by an electrostatic precipitator P, passes through a throttle valve V and into a 46-inch long wooden box B, then passes through a 50-inch diffuser of 6° half angle into a plenum chamber C 36 inches long and 12 inches in diameter. The wooden box contains two plastic grids for mixing purposes, and there are two fine screens in the plenum as shown. The use of the loudspeaker L is described in §3. A nozzle N having a 12:1 diameter contraction was used for the present flow-visualization experiments, the exit diameter D of the jet being 1 inch (the schematic shows a 2-inch jet used for later hot-wire studies). A laminar boundary layer surrounds the jet column, which emerges with a top-hat velocity profile and a 0.1% turbulence level. The jet can be driven up to a speed U_e of about 220 ft/sec.

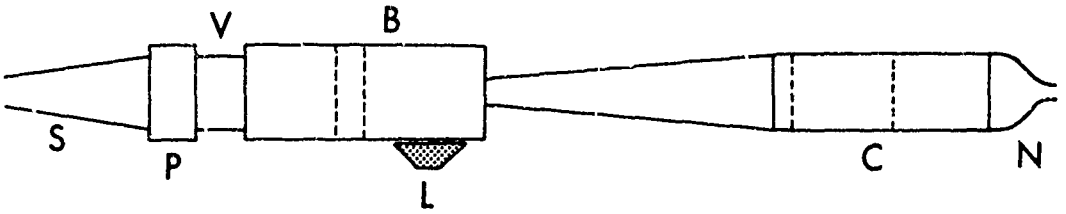

Figure 3. Schematic of the jet facility, which is about 16 ft long. The dotted lines represent grids or screens, and the labeled parts are described in the text.

In consideration of ambient room drafts, we decided not to run the jet below 20 ft/sec, corresponding to a Reynolds number Re of about 10,000, where $Re = U_e D/\nu$, and ν is the kinematic viscosity of air. We therefore could not explore the Reynolds-number range 1000-10,000, but fortunately excellent photographs have been taken in that range by Brown (1935) of a two-dimensional jet and by Becker & Massaro (1968) of the axisymmetric case. Becker & Massaro observed axisymmetric waves on the jet column for Reynolds numbers up to about 10,000, beyond which the flow appeared to degenerate into chaos. Their nozzle was fed by a long pipe, however, having a diameter only 3.8 times that of the jet. It is easy to show from continuity that the Reynolds number of the pipe would have been 10,000/3.8 = 2600 based on mean flow speed, when the Reynolds number of the jet itself was 10,000. Natural transition in a pipe occurs at a Reynolds number of about 2600, so the loss of order may have been caused by transition upstream of the nozzle.

Figure 4(a) is a schlieren spark photograph of our air jet under the conditions D = 1 inch, U_e = 36 ft/sec, and Re = 18,700. The photographic technique was similar to that of Bradshaw *et al* (figure 1) except that the jet was seeded with CO_2 rather than Freon and the knife edge was vertical instead of horizontal. The spark duration was about 2 μsec, and high contrast Type 51 Polaroid film was used. The flow within the first four diameters of the nozzle is dominated by organized axisymmetric structure, including short interfacial waves near the nozzle, and two large-scale puffs further downstream. The puffs look rather like the underlying structure one seems to discern in figure 1. If orderly structure exists

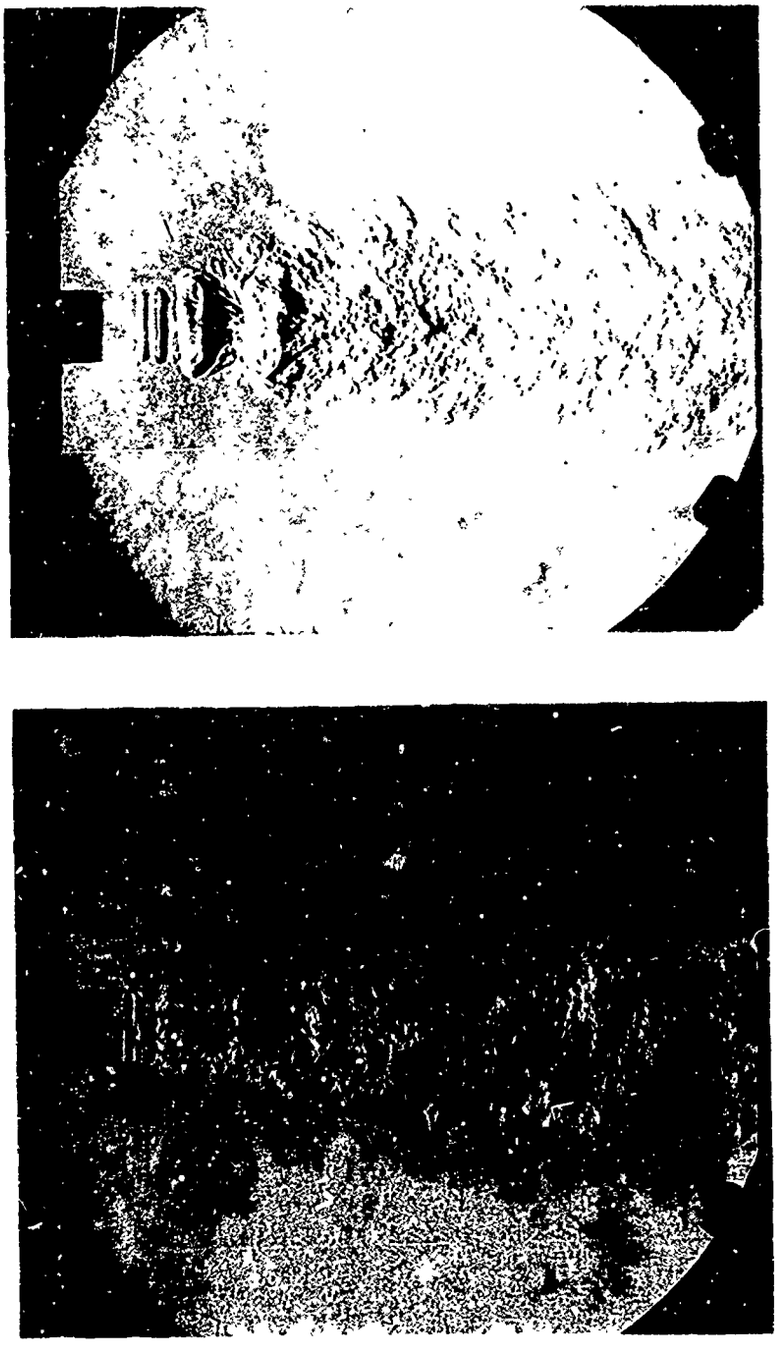

Figure 4. Schlieren photographs of the 1-inch air jet, made visible by CO_2 at Reynolds numbers of (a) 18,700 and (b) 52,700.

beyond the first four diameters, it is obscured by a finely textured sheath of CO_2. Figure 4(b) is a similar photograph taken under the conditions U_e = 102 ft/sec and Re = 52,700. The ripples on the laminar boundary layer have shortened but are still clearly visible. Any large-scale structure that may exist downstream, however, is masked by a fine-grained mixture of CO_2 and air surrounding the jet. A schlieren image emphasizes fine detail, though not nearly so much as a shadowgraph. Jet-noise production, on the contrary, is heavily biased toward large-scale eddies (Ffowcs Williams 1963). We needed another method of visualization to search for large-scale order at higher Reynolds numbers.

After investigating several types of smoke, each of which was noxious, corrosive, or dirty, we settled upon fog as the flow-visualization medium. The fog was made by injecting steam into the airflow and passing the mixture over pans of liquid nitrogen in the box B of figure 3. By a judicious choice of the pan area and grid geometry inside the box, we could produce a light fog without freezing the plenum screens. The temperature of the fog was about 50°F. Air saturated at 50°F is 1.03 times denser than dry room air at 70°F, so the jet column was only about 3% denser than its surroundings. Figure 5 is a photograph of the facility, as outfitted for high-speed motion picture photography. The 1-ft diameter jet plenum is suspended inside a 2-ft diameter chamber containing several more pans of liquid nitrogen. They served to refrigerate the skin of the plenum, for otherwise the jet would emerge with a warm and fog-free boundary layer. Note the crossed lighting and blackened screens, necessary because fog scatters light efficiently only in directions more-or-less

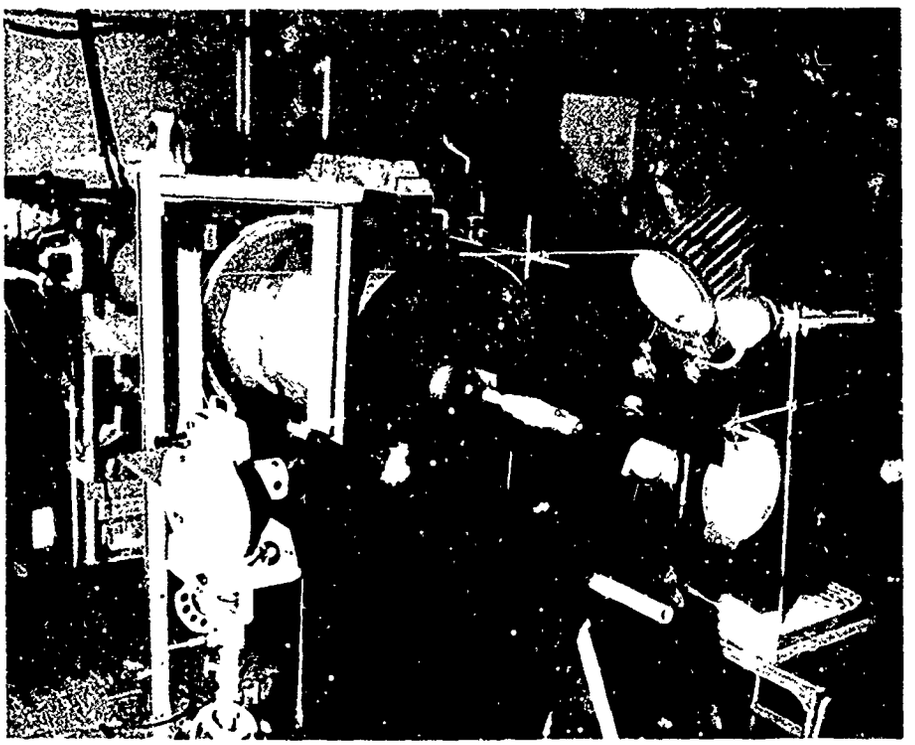

Figure 5. The fog-seeded jet, as outfitted for high-speed motion picture photography.

forward. The arrangement for stills was similar except that a single xenon flash lamp provided the illumination. The duration of the flash was measured as 20 μsec, brief enough for an unblurred image at the highest speeds tested.

Figure 6 comprises seven photographs of the 1-inch fog jet at exit speeds ranging from 20 ft/sec to 147 ft/sec. The corresponding Reynolds numbers advance from 10,500 to 75,700 in roughly equal increments. Some idea of the relation between the schlieren and light-scattering methods of visualization can be gained by comparing figures 4(b) and 6(e), both of which were taken around Re = 52,000. The schlieren picture 4(b) clearly shows the short waves that grow on the vortex sheet immediately downstream of the nozzle, but large-scale structure further down is left mainly to the imagination of the viewer. The fog picture 6(e) shows two dramatic large puffs 2-5 diameters downstream but cannot resolve the fine ripples near the nozzle. The large-scale puffs were photographed regularly up to the Reynolds number of 65,200, were infrequent at 75,700, and were not observed in such a striking form above that.

Using the lighting arrangement shown in figure 5, we made motion pictures of the fog jet at frame rates ranging from 5000 to 11,000 per second. After a careful study of the motion pictures and of the fog and schlieren stills, we came to the tentative conclusion that a jet experiences two kinds of orderly process within the range of Reynolds numbers under consideration: an instability of the thin laminar boundary layer leaving the lip, and a much larger-scale process of puff formation further downstream. The instability scales on the thickness of the boundary layer, whereas puff

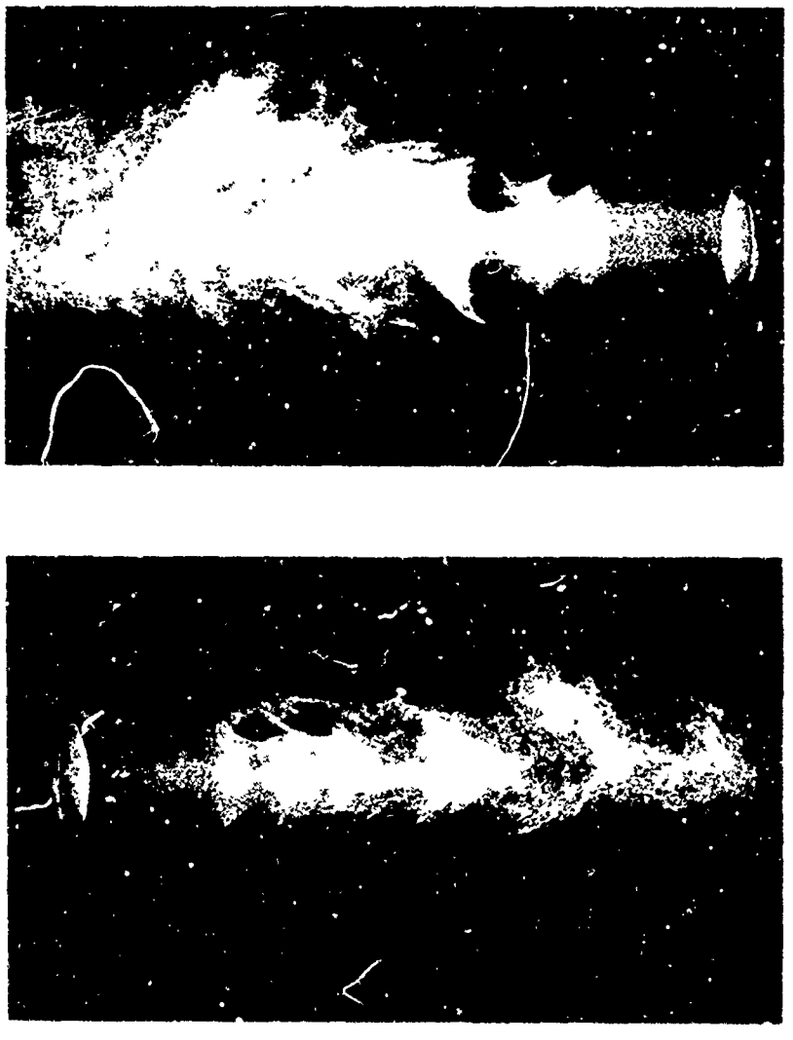

Figure 6. Spark photographs of the 1-inch fog jet. The Reynolds numbers range from 10,500 to 75,700 as follows: (a) 10,500, (b) 19,500, (c) 30,900, (d) 43,500, (e) 51,400, (f) 65,200, and (g) 75,70

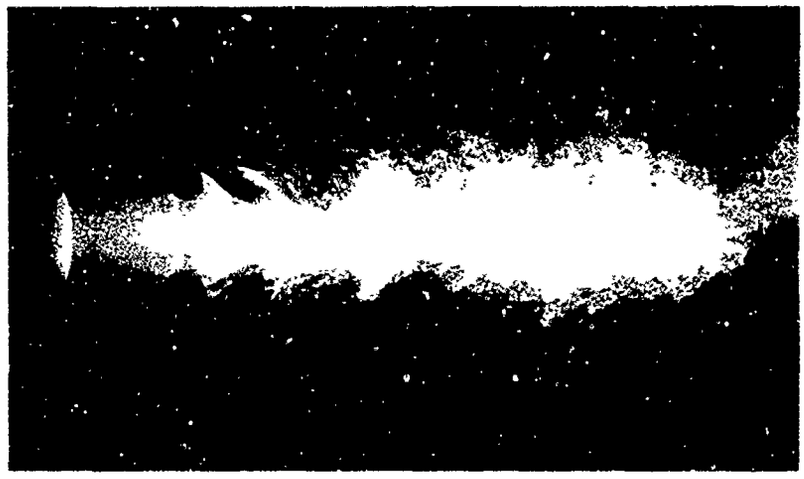

(c)

(d)

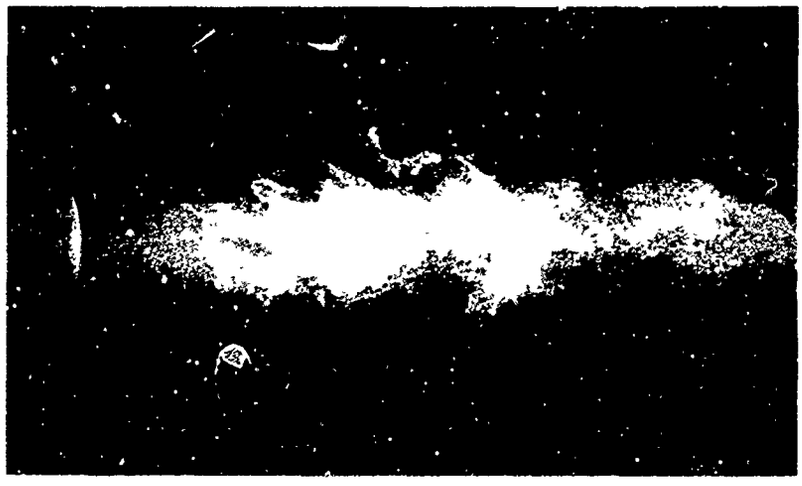

(e)

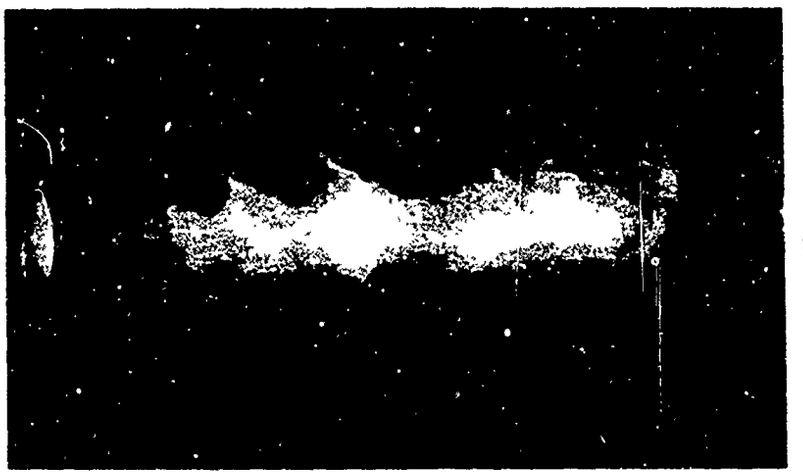

(f)

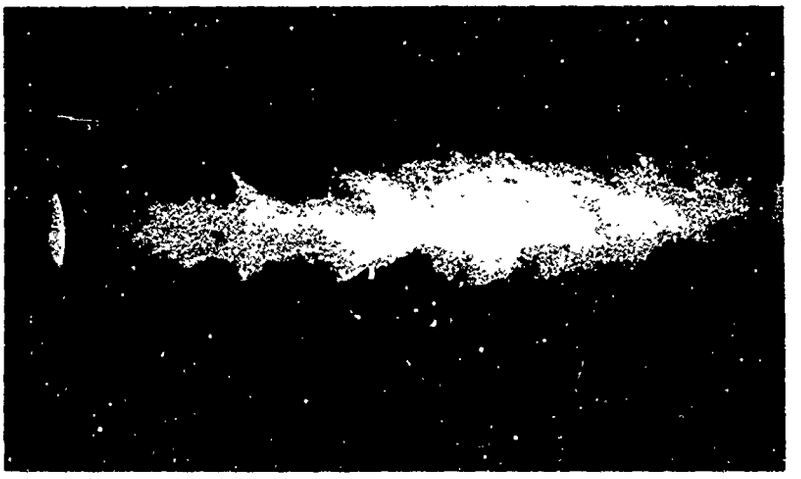

(g)

Figure 6 continued.

formation involves the whole jet column and scales on its diameter.

The boundary-layer instability has been studied extensively, in particular by Sato (1960) and Browand (1966), and especially in a definitive sequence of papers put forth by Wille (1952) and his colleagues at the Deutsche Versuchsanstalt für Luft-und Raumfahrt in Berlin. Bibliographies of that work are given in a review by Michalke & Wille (1966) and in one of the later papers in the sequence by Freymuth (1966), who presents photographs obtained by a method suited especially for visualizing short waves downstream of a lip.

The work of the Berlin school concerns a free boundary layer sufficiently thin that the diameter D of the jet has no influence on the instability. In that limit the boundary layer behaves much like the two-dimensional vortex sheet of classical inviscid stability theory. The finite thickness of the boundary layer, however, distinguishes a wavelength at which the instability grows at a maximum rate. For a hyperbolic-tangent velocity profile having a thickness δ based on maximum slope, Michalke (1964, 1965) showed theoretically that the wavelength λ for maximum *temporal* growth is 7.07 δ, and that the wavelength for maximum *spatial* growth is 7.80 δ. The phase velocity of the preferred temporally growing wave is exactly one-half U_e, whereas the phase velocity in the case of spatial growth is 0.513 U_e.

We made hot-wire surveys of the laminar boundary layer leaving our jet at various Reynolds numbers and found that the profile relaxes quickly into a hyperbolic-tangent form. Results for the thickness δ based on maximum slope at a distance 0.02 inches downstream are presented in the

table below, together with values of the wavelength λ measured from the photographs:

Table 1. Boundary-layer thicknesses and instability wavelengths in dimensionless form.

Re	δ/D	$(Re)^{\frac{1}{2}}\delta/D$	λ/D	λ/δ
10,500	0.041	4.16	0.44	10.9
19,500	0.031	4.34	0.24	7.7
30,900	0.025	4.36	0.19	7.6
51,400	0.020	4.47	~0.14	~7

It is clear from the second column of the table that the boundary layer is thin compared with the diameter of the jet, so the work of the Berlin school would be expected to apply. The third column shows that δ/D varies approximately as $(Re)^{-\frac{1}{2}}$ in accord with simple viscous boundary-layer concepts. The constant of proportionality, ~4.4, of course depends on the geometry of the nozzle and should decrease with decreasing contraction ratio (cf. equation 1 of Becker & Massaro 1968). The fourth column of table 1 shows that λ is fairly small compared with D except possibly at the lowest Reynolds number studied. Save at that Reynolds number the waves are approximately two-dimensional, and the fifth column shows that λ/δ does indeed have values between 7 and 8 in accord with the stability theories of Michalke (1964, 1965). Phase velocities measured from the motion pictures were about 0.5 U_e as well. These data are not nearly so accurate as

those of Freymuth (1966), who used a loudspeaker to drive the instability so that phase velocities and growth rates could be measured accurately. Table 1 is intended to show that the boundary-layer instability seen in our photographs is the two-dimensional phenomenon studied by the Berlin school and that the maximally amplified mode arises without artificial excitation.

The short waves quickly steepen and combine pair-by-pair into longer waves, the subharmonics measured by Browand (1966) and Freymuth (1966). That terminates the evolution of orderly structure at a Reynolds number of 10,500, and the subharmonic waves propagate on downstream, gradually losing their coherence without much change in overall shape [figure 6(a)]. As the Reynolds number advances toward 20,000, a second and rather more violent combination follows the first so that four waves become packed, so to speak, into a puff. As the Reynolds number advances still higher, a cascade of pair-by-pair combinations occurs, initiated by surface waves of decreasing length, and terminated by a train of puffs as seen in figure 6. The structure of the train is relatively insensitive to Reynolds number, as though the cascade seeks a terminal state defined only by U_e and D.

The puffs are more sporadic than the initial ripples. Three or four puffs form and induct themselves downstream, an interval of confused flow ensues, several more puffs form, and so on. Formation is not periodic, but *average* frequencies f could be found simply by counting puffs during screenings of the flow-visualization motion pictures. A count depends to a certain extent on what one chooses to interpret as a "puff", but the results have some objectivity as demonstrated by the table of timed counts

below:

Table 2. Average Strouhal numbers of puff formation.

Re	Subject SCC	Subject SFC	St
10,500	50	48	0.29
19,500	55	51	0.32
30,900	60	63	0.28

Subject SCC was one of us, and subject SFC was an observer without technical training, instructed briefly beforehand about the nature of a "puff". The agreement between the counts presented in the second and third columns is limited evidence that the puffs exist as an objective terminal state of orderly flow. Average Strouhal numbers based on the puff counts, $St = fD/U_e$, are shown in the fourth column and are seen to have values around 0.3 independent of the Reynolds number over the very limited range considered. Accurate counts at higher Reynolds numbers could not be obtained, because lighting limitations and the high frame rates required to avoid blurring (8000 per second and above) resulted in films of poor quality, lacking some of the visual cues that facilitated the counts shown. The still pictures of figure 6 imply that structural similarity extends to Reynolds numbers much higher than 30,900.

In the course of watching the motion pictures, we came to understand why a conventional shadowgraph reveals no large-scale structure in jet turbulence. Some foggy air is thrown out of the jet column as each puff

forms. While the puff inducts itself downstream, the ejected fog remains behind as a passive sheath around the column. Although dynamically unimportant, the sheath shows up clearly in a schlieren picture and would dominate a shadowgraph completely. A final observation from the motion pictures: for the Reynolds numbers under consideration, the conical potential core of the jet is the *interior envelope* of the waves growing on its surface.

3. Means of Forcing the Jet

The photographs led us to imagine turbulence in the transitional region of a jet as a *vortex train*, a train of loosely packed vortex rings only weakly dependent on the circumstances of their origin. The idea is attractive, because a vortex ring is a much more stable state of flow than a columnar vortex sheet. The sheet can plausibly be expected to wrap into a train of vortex rings carrying the same momentum, each ring maintaining its identity some distance downstream from its point of origin. One can easily show that a train of vortex rings would distort a fog column into spade-shaped puffs of the kind seen in figure 6.

The wake of an aircraft is known to follow a similar course (Crow 1970). An aircraft generates a pair of trailing vortices, which undergo a symmetric instability driven by their mutual induction, until they connect at points to form a train of vortex rings oriented parallel to the ground. The rings are quasi-stable, preserving a degree of order intermediate between the original vortex pair and the chaos that finally

unfolds. Because of its stability, the vortex ring may be a common if not universal mode of transitional flow.

The visual evidence for order in jet turbulence becomes ambiguous at a Reynolds number around 70,000, beyond which we were unable to produce a photograph better than figure 1. The vortex puffs seen in figure 6, moreover, are fed by a laminar instability, and the question remains whether they would exist in the absence of a laminar boundary layer. The Strouhal number 0.3 associated with puff formation is affirmative evidence, since the peak of the jet-noise spectrum lies between 0.25 and 0.30 depending on angle from the jet axis. The coincidence suggests that the vortex train is latent in jet turbulence at high Reynolds numbers and contributes to the emission of sound.

The hypothesis of latent order can be tested in at least two ways. One way would be to extract the mode of greatest likelihood from hot-wire signals, along the line advocated by Lumley (1966) and commonly used by electrical engineers to extract signals from non-white noise. We adopted the alternative, however, of forcing the jet periodically and measuring the response. If there were no latent order in the unforced case, then the result of forcing would be damped waves analogous to those studied by Hussain & Reynolds (1970) in turbulent channel flow. If there is a natural tendency toward order, then periodic forcing may raise the latent structure above background turbulence and permit measurements without complicated signal-extraction procedures.

For the purposes of such experiments, the apparatus was modified in three ways: the diameter of the jet was increased to 2 inches, the

boundary layer was tripped just upstream of the exit, and a loudspeaker was attached to the wooden box previously used for mixing fog. Doubling the exit diameter raised the operational Reynolds number of the jet to 100,000, corresponding to an exit speed of about 100 ft/sec. The blower can drive the 2-inch jet up to 145 ft/sec, but the higher speed was reserved for hot-wire calibration. The jet has a top-hat velocity profile and a 0.3% turbulence level, higher than in the 1-inch jet, because the nozzle contraction is halved. In the absence of a trip, the boundary layer surrounding the 2-inch jet column is laminar and has a thickness $\delta = 0.022$ inches at an exit speed $U_e = 100$ ft/sec.

We tripped the boundary layer to achieve a measure of Reynolds-number independence and especially to destroy short interfacial waves immediately downstream of the nozzle. The trip ring fits tightly into the 2-inch nozzle about 1 inch upstream from the exit. Deep axial notches cut into the ring forestall any organized vortex shedding on its part. The ring is 0.140 inches long and 0.020 inches thick, about as thick as the laminar boundary layer just upstream of the ring when $U_e = 100$ ft/sec. At that speed the tripped boundary layer is intensely turbulent, with a peak root-mean-square axial fluctuation of $0.079\ U_e$. The thickness of the turbulence intensity distribution at half its peak value is 0.062 inches, about 6% of the nozzle radius. The boundary layer becomes untripped at an exit speed of about 40 ft/sec, much lower than any used in the present experiments. Above 40 ft/sec, the jet is invariant to Reynolds number with respect both to mean and to root-mean-square quantities, as far as can be determined from the limited range of accessible Reynolds numbers.

Figure 7 is a plot of the mean axial speed U measured on the centerline at various positions x and at four Reynolds numbers Re. The coordinates represent the dimensionless quantities U/U_e and x/D. The circles are data at Re = 103,000, and data at other Reynolds numbers are plotted wherever they do not overlap the circles. The mean axial profiles are practically indistinguishable in the Reynolds-number interval 62,000 to 124,000. Figure 8 is a similar plot of the turbulence intensity u, the root-mean-square axial component of turbulent velocity as measured on the centerline. A factor-of-two change in Reynolds number is seen to have little effect on the ratio u/U_e. The curves in figures 7 and 8 are superposed on later plots to represent the unforced state. Hopefully the tripped boundary layer resembles conditions at the exit of a turbojet engine, but certainly the boundary layer is fully turbulent and sustains no orderly oscillations of its own. Any large-scale structure that can be evoked has nothing to do with details of the boundary layer shed from the nozzle.

The loudspeaker L sketched in figure 3 provided the forcing. The 12-inch diameter loudspeaker was installed upstream of the plenum to keep the exit conditions clean. As a result, the transmission of energy between the loudspeaker and the exit plane is efficient only at certain discrete forcing frequencies, which are the organ-pipe resonances of the cavity. As far as internal acoustic waves are concerned, the highly contracted nozzle presents a closed face and is therefore a pressure maximum at resonance. The oscillating pressure upstream of the contraction results in an oscillating speed at the exit, since the jet must attain the constant ambient

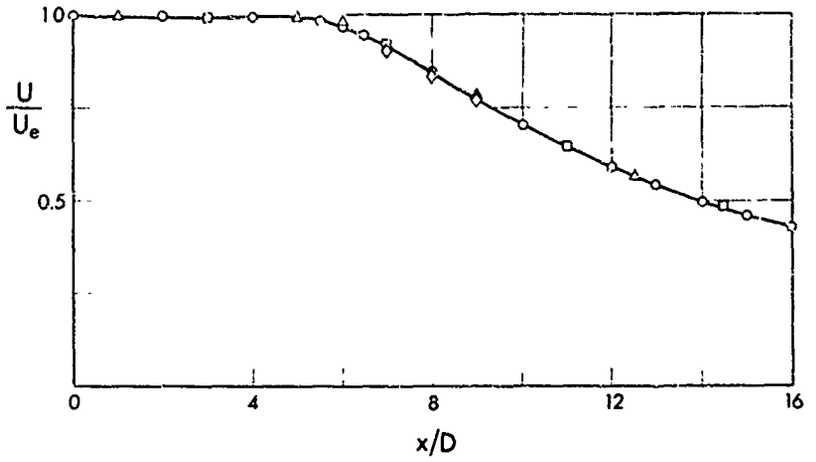

Figure 7. Profile of the mean axial speed on the centerline at several Reynolds numbers, as denoted by the following data symbols: △ 62,000, □ 83,000, ○ 103,000, and ◇ 124,000.

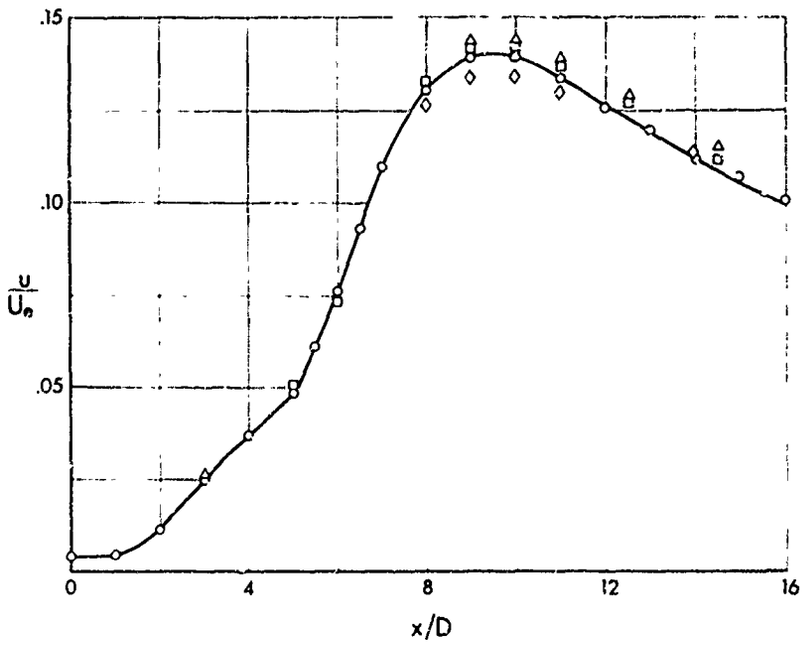

Figure 8. Profile of the root-mean-square axial fluctuation on the centerline The data symbols are defined in the caption of figure 7.

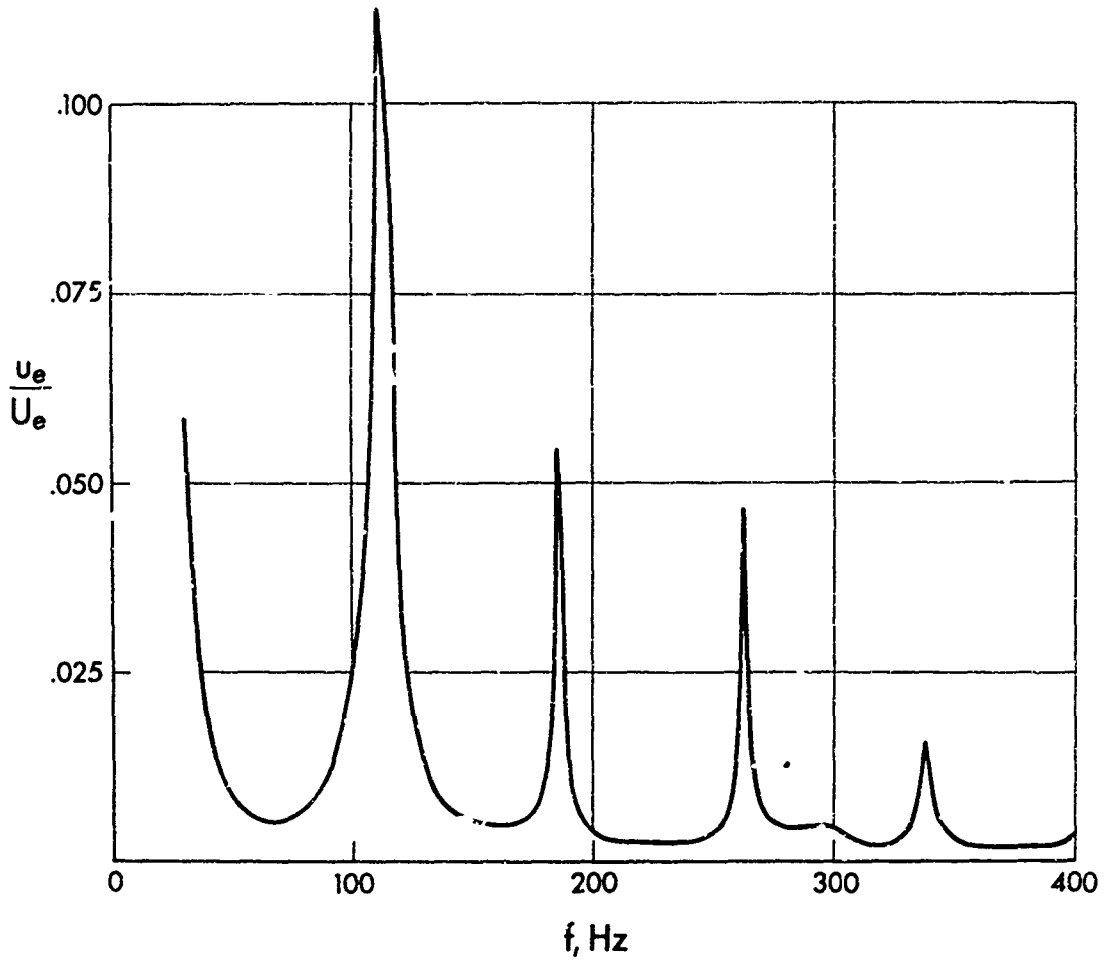

Figure 9. Spectrum of the jet cavity, measured in terms of the root-mean-square surging in the exit plane.

pressure downstream of the contraction. Figure 9 is a spectrum of the jet cavity, measured at an exit speed U_e = 60 ft/sec, with a root-mean-square potential W = 10.5 V across the terminals of the loudspeaker. The abscissa is frequency f, and the ordinate is u_e/U_e, where u_e is the root-mean-square sinusoidal speed fluctuation at the jet exit, as measured by a hot-wire anemometer. The spectrum has resonance peaks at f = 113 Hz, 185 Hz, 262 Hz, and so on. The resonance frequencies are independent of U_e, but the surging amplitude u_e/U_e at a particular resonance is proportional to W/U_e^2, a result that can be deduced by assuming the fluctuating pressure upstream of the contraction to be proportional to W and applying Bernoulli's equation to the contraction process itself.

We wanted to find how the jet responds to periodic surging at Strouhal numbers ranging from 0.15 to 0.60, from half to twice the Strouhal number of 0.3 derived from puff counts. Among the quantities in the definition $St = fD/U_e$, D was fixed at 2 inches, f could take on discrete values, and U_e could be varied continuously. Varying U_e, however, would result in simultaneous changes of the Reynolds number $Re = U_eD/\nu$. Although the boundary-layer trip makes the flow insensitive to Reynolds number, we chose to hold Re near 100,000 by skipping from one resonance to the next according to the following schedule:

Table 3. Forcing frequencies, exit speeds, and Reynolds numbers of the hot-wire experiments.

St	f (Hz)	U_e (ft/sec)	Re
0.15	113	126	130,000
0.20	113	94	96,900
0.25	113	75	77,500
0.30	185	103	106,000
0.35	185	88	90,700
0.40	262	110	112,700
0.45	262	97	99,800
0.50	262	87	89,800
0.55	262	79	81,700
0.60	337	94	96,400

Each of the experiments described in subsequent sections was performed at the conditions specified in a row of table 3. The Reynolds-number variations are unimportant, and the periodic surging can be described in terms of a Strouhal number St and dimensionless root-mean-square amplitude u_e/U_e. Notice that the frequencies in table 3 correspond to sound waves 3-10 ft long inside the cavity. The jet turbulence outside does not interact directly with such waves and remains incompressible. The effect of the internal waves is to impose a periodic fluctuation on the strength of the vortex layer leaving the nozzle.

We measured several kinds of response downstream, each based on

the axial component of velocity: the mean speed U; the root-mean-square axial fluctuation u; root-mean-square fluctuations $u_{0.30}$, $u_{0.60}$, filtered around Strouhal numbers denoted by the subscripts; the spectrum F(f) of the axial fluctuation; the length λ and phase velocity c of organized waves. Most measurements were made on the centerline of the jet. In more general cases the cylindrical coordinates (x,r) of the hot wire are given, r = 0 being the centerline of the jet and x = 0 the exit plane.

Signals were obtained by means of a linearized, constant temperature Disa anemometer. The mean speed U resulted from analogue integration over an interval typically 100 sec. The root-mean-square fluctuation u was measured with a Disa r.m.s. voltmeter, having a response flat to within 1% of full scale for all frequencies between 1 and 100,000 Hz. The core of the experiments is to relate the dimensionless turbulence intensity u/U_e to the axial location x/D and to the input variables u_e/U_e and St. The jet is to be regarded as a "black box", a nonlinear oscillator whose properties are to be understood in terms of the inputs u_e/U_e, St and response u/U_e.

Now that the relevant parameters have been defined, it is worth noting exactly how this study fits with previous work involving loudspeaker excitation of jets. We deal with Reynolds numbers Re $\approx$ 100,000, about ten times *higher* than those explored by Becker & Massaro (1968). We deal with Strouhal numbers St $\approx$ 0.30, about ten times *lower* than those explored by Freymuth (1966), who confined his study to high-frequency waves, much shorter than the diameter D of the jet. Freymuth defined his Strouhal number in terms of boundary-layer thickness, but the lowest value of fD/U_e

he reached was about 0.9 ($f\delta/U_e \approx 0.002$, figure 16, Freymuth 1966). A fundamentally new phenomenon arises as St descends below about 0.45: the forced wave becomes highly dispersive and attains an amplitude large enough to disintegrate the jet column.

4. Structure of the Preferred Mode

We begin by explaining the consequences of forcing at St = 0.30, which table 2 suggests as the Strouhal number of natural oscillation. Except for a large accessible amplitude, the mode driven at St = 0.30 is typical and serves as a useful introduction to the quantitative work.

The vortex puffs appear in the motion pictures to grow abruptly about four diameters downstream, just ahead of the tip of the potential core. On that basis, a strong response u/U_e would be expected at a point $x/D = 4$, under a surging imposed at St = 0.30. Figure 10 is an amplitude-response function measured under those conditions on the centerline of the jet. The abscissa is the forcing amplitude u_e/U_e measured at $x/D = 0$ and, incidentally, found to be uniform over the exit plane. The ordinate is the response u/U_e measured by moving the hot wire back along the jet axis to $x/D = 4$. The value $u/U_e = 0.038$ at $u_e/U_e = 0$ is the natural turbulence intensity near the tip of the potential core. The amplitude response is shaped like many response functions occurring in engineering, for example the stress-strain diagram for a ductile metal: the curve rises almost linearly with small forcing amplitudes, then yields, or saturates, under some nonlinear effect (of course the figure represents time-averaged rather

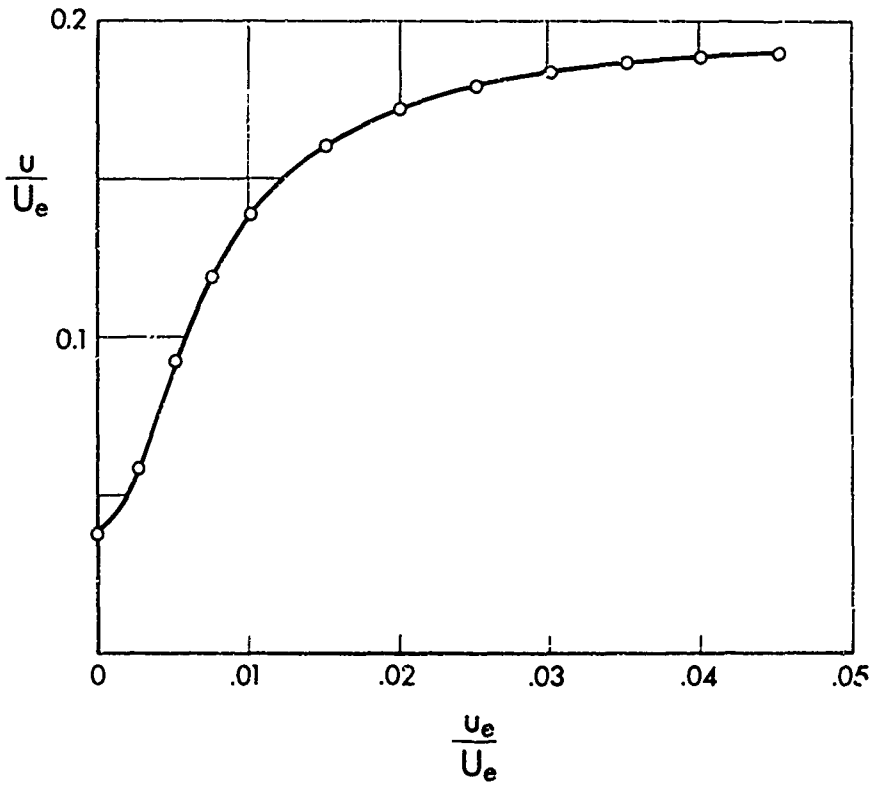

Figure 10. Amplitude response at the preferred Strouhal number 0.30. The response u/U_e is measured on the centerline four diameters downstream of the jet exit.

than instantaneous relationships). Under a forcing amplitude of 1%, that is $u_e/U_e = 0.01$, the response u/U_e is 13.9%, only a small part of which is aperiodic background turbulence (cf. figure 12). Under a forcing amplitude $u_e/U_e = 2\%$, the response u/U_e has risen to 17.2%, and it cannot be driven past 19% under any reasonable level of forcing.

One might have thought the waveform at x/D = 4 simply falls apart under forcing amplitudes above 1-2%, but quite a different process underlies saturation. Figure 11 shows four oscilloscope photographs of the waveforms upon which figure 10 is based. The forcing amplitudes u_e/U_e are 0.005, 0.01, 0.02, and 0.04, doubling from one photograph to the next. The amplitude and time scales are arbitrary but the same in all pictures; the axial component of velocity increases toward the vertical, and time increases from left to right. The signal at a forcing amplitude of 0.5% is a sine wave, distorted at random by ambient turbulence. As u_e/U_e advances to 1%, the signal becomes cleaner and almost doubles in amplitude, but still resembles a sine wave. The amplitude has increased only slightly at $u_e/U_e = 2\%$, but now the waveform has steepened along its rising front; a significant harmonic has arisen from the fundamental being forced. Since the Strouhal number of forcing is 0.30, the Strouhal number of the harmonic must be 0.60. Little change takes place as u_e/U_e increases from 2% to 4%, though some fine-scale turbulence begins to appear during the relaxing part of the wave cycle. The wave does not become disordered at forcing amplitudes above 1%, but instead saturates under the action of its harmonic.

Those remarks are given quantitative form in figure 12, which is a plot of *filtered* amplitude-response data. The curve without data points

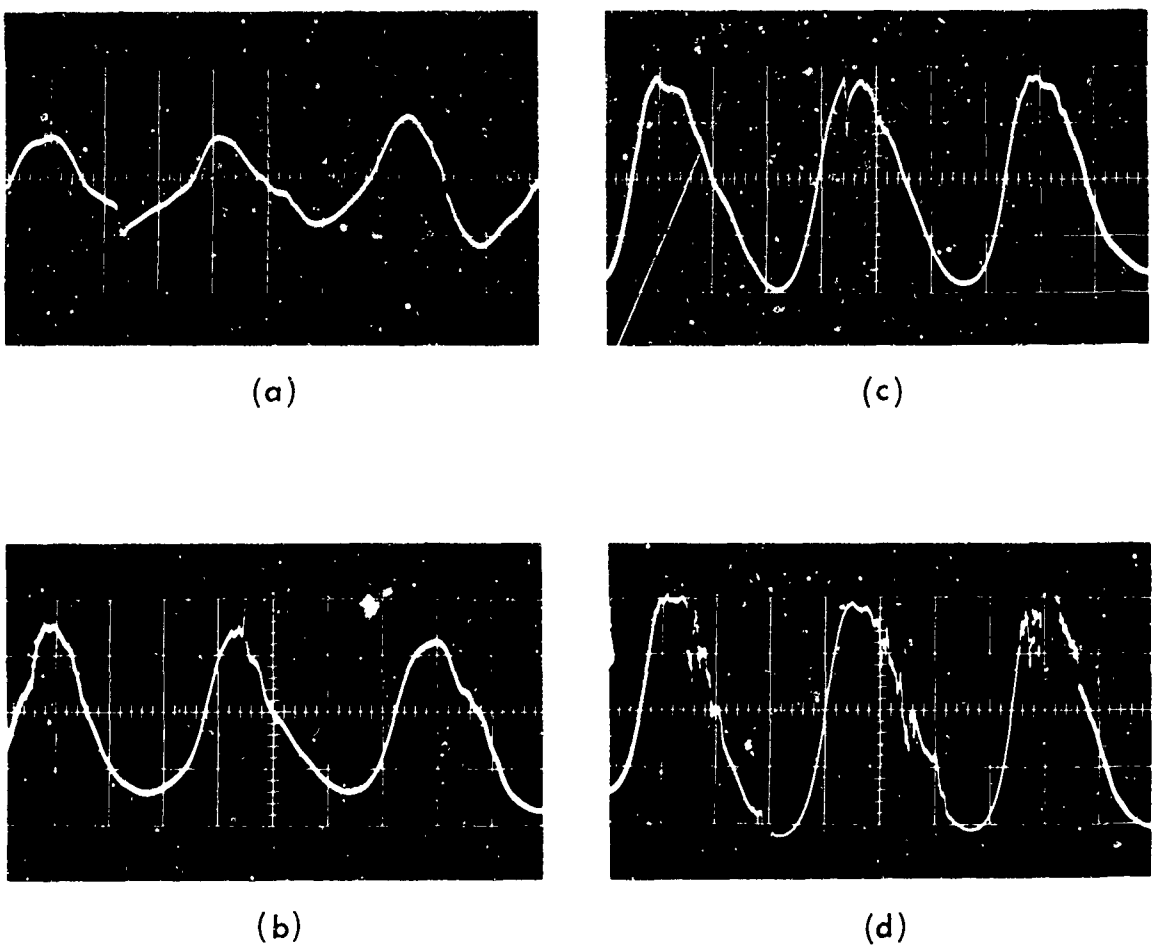

Figure 11. Waveforms of the preferred mode, measured on the centerline four diameters downstream of the exit. The Strouhal number is 0.30 and the forcing amplitudes u_e/U_e are (a) 0.5%, (b) 1%, (c) 2%, and (d) 4%.

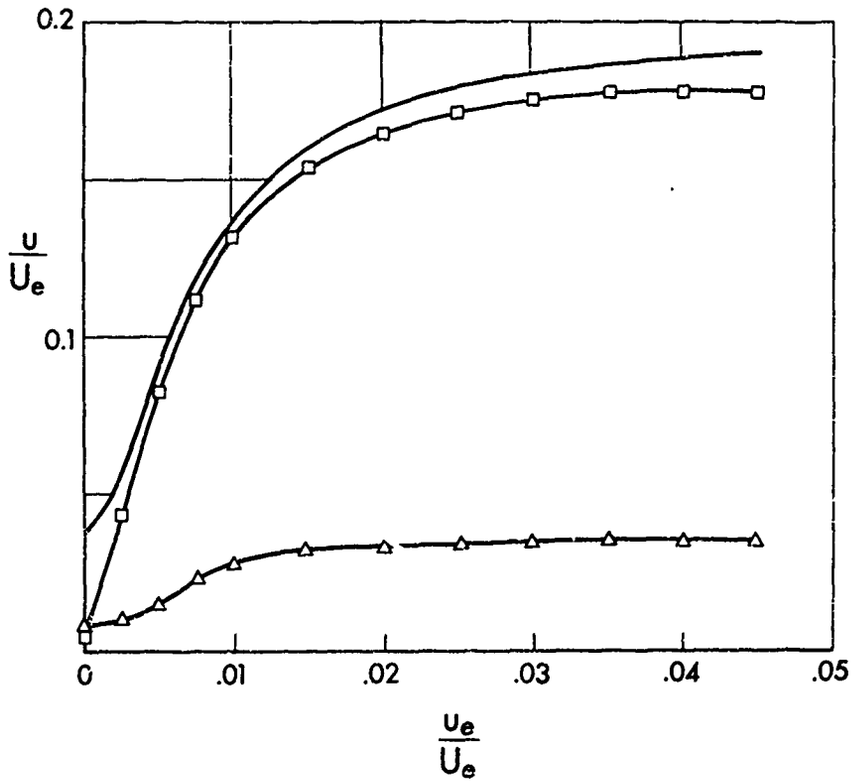

Figure 12. Filtered response functions of the preferred mode. The experimental conditions are the same as for figure 10, from which the curve without data points is taken, representing the total intensity u/U_e. The square data symbols denote the fundamental response $u_{0.30}/U_e$, and the triangular symbols denote the harmonic response $u_{0.60}/U_e$.

is the total amplitude response u/U_e taken from figure 10, the curve defined by the square data symbols is the fundamental response $u_{0.30}/U_e$ obtained by filtering the hot-wire output around the forcing frequency 185 Hz, and the curve with triangular symbols is the harmonic response $u_{0.60}/U_e$ obtained by filtering around 370 Hz. The filter was a Dytronics Model 720, with a band-pass width about 7% of the center frequency. The fundamental is accurately linear up to a forcing amplitude $u_e/U_e = 0.5\%$, then curves over as u_e/U_e increases from 0.5% to about 1.5%. The harmonic builds up in the same interval, and the two come into equilibrium around $u_e/U_e = 2\%$. The fundamental saturates at a value $u_{0.30}/U_e = 17.9\%$, and the harmonic at $u_{0.60}/U_e = 3.5\%$.

All the data presented so far were obtained on the centerline at $x/D = 4$, which was deemed likely to be the point of maximum response on the basis of the flow-visualization experiments. The conjecture can be verified by fixing u_e/U_e and varying the hot-wire location x/D. Figure 13 is an axial profile of the fluctuation intensity u/U_e, measured along the centerline under the forcing conditions $u_e/U_e = 2\%$ and $St = 0.30$. The intensity profile for the unforced case is superposed from figure 8 without data points. The slight but well chosen surging at the exit plane is seen to drive a powerful wave, which indeed reaches a peak amplitude near $x/D = 4$, more precisely, at $x/D = 3.7$. The intensity profile decreases from $x/D = 4$ to 6 and there merges with the profile that exists in the absence of forcing. The natural turbulence intensity profile reaches a peak at $x/D = 9.5$ on the centerline, and forcing under the conditions $u_e/U_e = 2\%$, $St = 0.30$ draws that peak inward to $x/D = 8.5$.

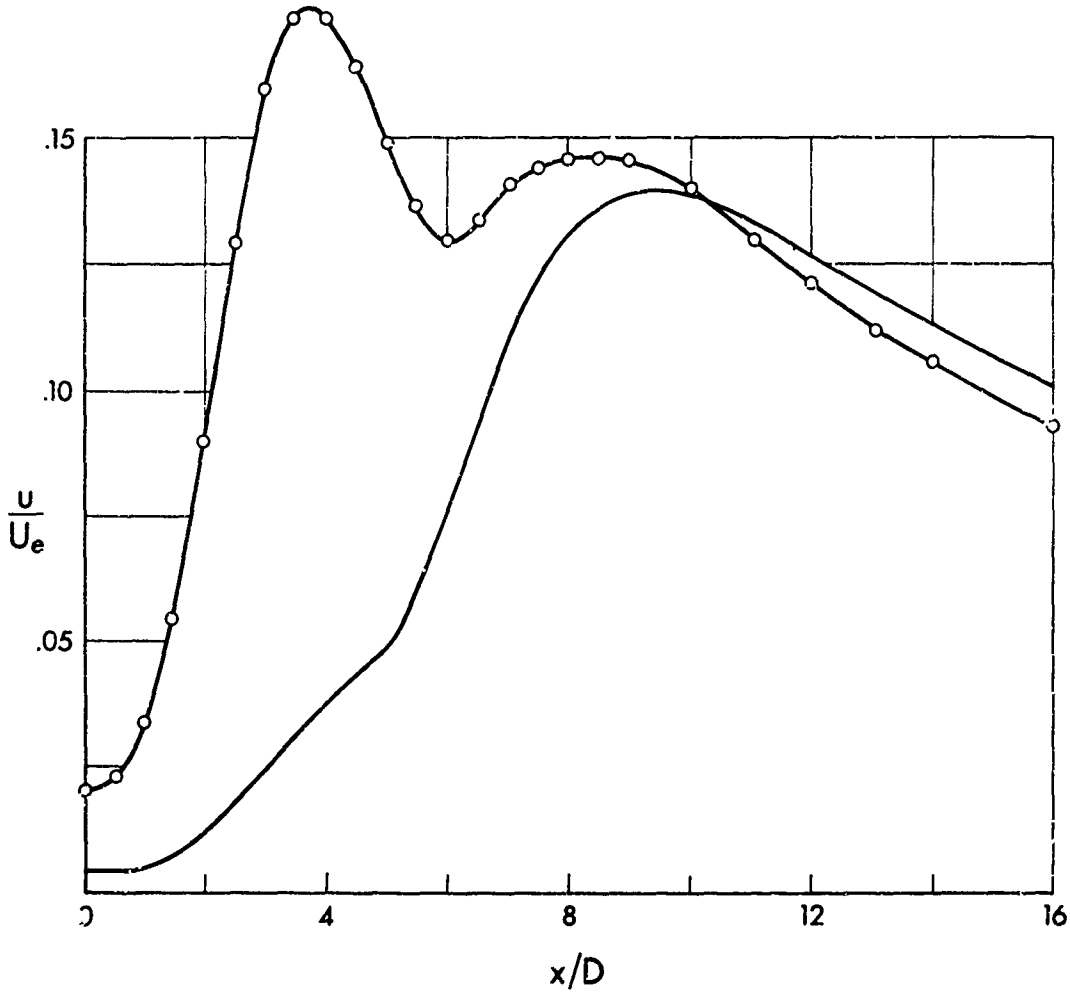

Figure 13. Axial profile of the turbulence intensity, measured along the centerline under 2% forcing at a Strouhal number of 0.30. The curve without data points represents the unforced case and is taken from figure 8.

Axial profiles of the root-mean-square filtered fundamental $u_{0.30}/U_e$ and harmonic $u_{0.60}/U_e$ are presented in figure 14 for the same forcing conditions. The fundamental and harmonic rise and fall together, with no apparent tendency for the spatial growth of the harmonic to lag the growth of the fundamental. Together they dominate the first six diameters of the jet and then fall toward zero. The experimental points do not quite reach zero, because the finite filter window admits some background turbulence not being driven by the periodic surging, especially in the intensely turbulent region around x/D = 8. The total intensity u/U_e is reproduced without data points in figure 14 as a solid line. The dashed line is the residual obtained by subtraction of squares:

$$\frac{u_r}{U_e} = \left\{ \left(\frac{u}{U_e}\right)^2 - \left(\frac{u_{0.30}}{U_e}\right)^2 - \left(\frac{u_{0.60}}{U_e}\right)^2 \right\}^{1/2} .$$

The intention was to include only the periodic parts of the filtered terms, so the fundamental and harmonic curves in figure 14 were extrapolated sensibly to zero near x/D = 8 before the subtraction.

If the remaining harmonics of the forced wave are small, as seems likely, the u_r/U_e can be regarded as the intensity of background turbulence not under the control of the surging at the exit plane. The level of uncontrolled fluctuations on the centerline is essentially zero from x/D = 0 to 3 and reaches the level of the controlled structure only at x/D = 6 under the forcing conditions u_e/U_e = 2%, St = 0.30. The energy in the curious ramp-like portion of the natural intensity profile, seen in

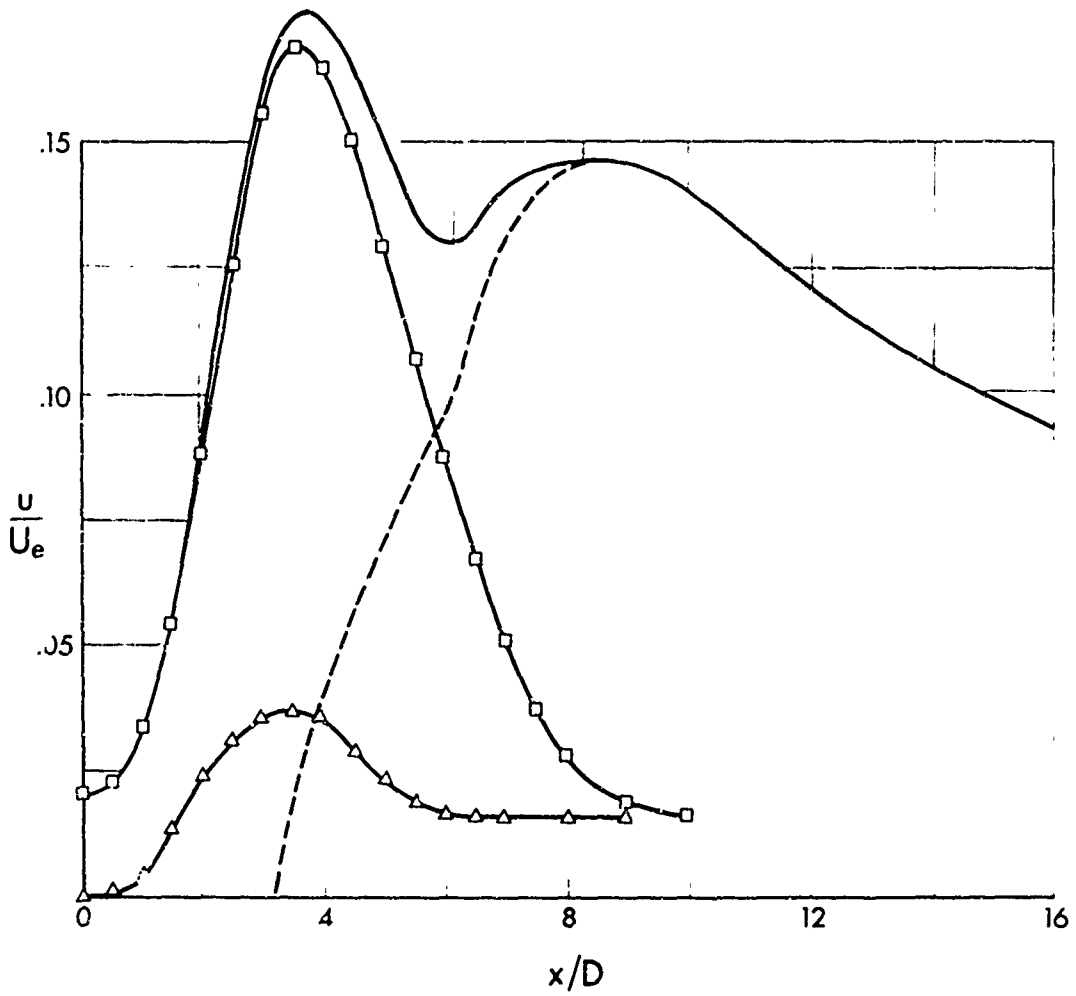

Figure 14. Filtered axial profiles of the preferred mode. The solid curve without data points represents the total intensity u/U_e and is taken from figure 13. The square data symbols denote the contribution $u_{0.30}/U_e$ of the fundamental, and the triangular symbols denote the contribution $u_{0.60}/U_e$ of the harmonic. The dashed curve represents the intensity of turbulence not bound in the fundamental or harmonic.

figure 8 between x/D = 0 and 5, is bou d into the strictly periodic flow. Presumably that ramp is the potential-core signature of big eddies in the mixing layer, in which case one can say that *big eddies within the first five diameters of the jet can be controlled by a slight surging applied in the exit plane at a Strouhal number of 0.30.* Moreover, *no control is possible beyond eight diameters.* By control, we mean that the surging fixes the frequency and phase of big-eddy formation.

The forced wave naturally has an effect on the mean flow. A complete discussion is deferred to §8, but an idea of the effect can be gained from figure 15, which is a profile of the dimensionless mean speed U/U_e measured on the centerline under the conditions u_e/U_e = 2%, St = 0.30. The line without data points denotes the unforced case, this time taken from figure 7. Forcing draws the asymptotic decay curve beyond x/D = 8 in toward the origin about two diameters. The reason for the shift in virtual origin is that forcing increases the entrainment between x/D = 0 and 8, so the jet passes out of the controlled region with a volume flux appropriate to an unforced jet leaving an exit two diameters upstream from the actual exit.

5. Amplitude Response at Various Strouhal Numbers

In what sense is the mode studied in the foregoing section preferred? We first considered the question during the flow-visualization experiments, when it became apparent that puffs tend to form at an average Strouhal number of 0.3. An obvious possibility is that St = 0.30 characterizes a

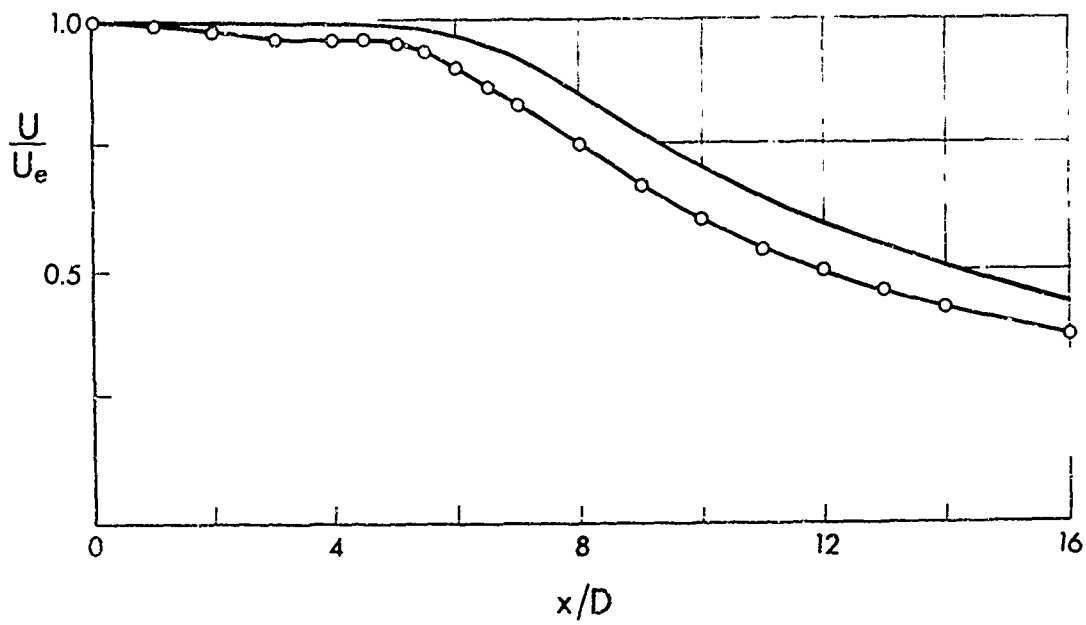

Figure 15. Effect of the preferred mode on the decay of mean speed along the centerline. The forcing level is 2%, and the Strouhal number is 0.30. The profile without data points represents the unforced case and is based on figure 7.

maximally amplified mode of linear instability, but the possibility does not survive analysis. Batchelor & Gill (1962) have treated the temporal instability of doubly infinite jet columns. For a top-hat velocity profile, they found that axisymmetric waves become progressively more unstable as the Strouhal number increases. Nothing seems to distinguish the mode at St = 0.30. If the column is presumed to have a boundary layer of finite thickness, then a two-dimensional mechanism (Michalke 1964, 1965) takes over and establishes a preference as the wavelength becomes comparable to the boundary-layer thickness. The fastest growing short waves are pitched much higher than St = 0.30, however, and in any case the boundary-layer trip has eliminated them from the present experiments.

We thought about other linear mechanisms outside the theory of Batchelor & Gill. Their theory was revised for spatially growing waves, purely oscillatory in time, but the amplification rate again was found to grow monotonically with Strouhal number (cf. §9). Spatial instability of a vortex sheet leaving a semi-infinite plate was studied (Orszag & Crow 1970), in the hope that an instability downstream of a jet might interact with the nozzle to produce a large local surging when St = 0.30. The interaction between a two-dimensional vortex sheet and an adjoining boundary was found to be disappointingly weak, however, and the interaction between a jet column and nozzle is probably even weaker. Every appeal to linear dynamics failed to establish a preference for the Strouhal number of 0.30. The reason is that nonlinearity establishes the preference.

Figure 16 is a plot of amplitude-response functions measured on the centerline at x/D = 4. The total response u/U_e is plotted against the

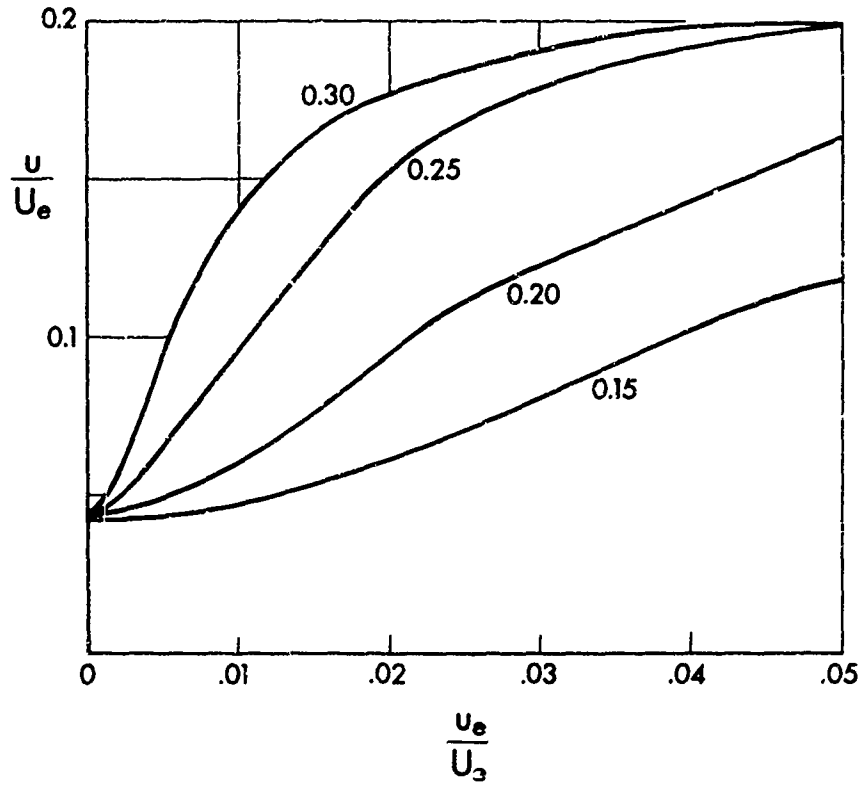

Figure 16. Amplitude-response functions measured on the centerline four diameters downstream of the jet exit. The response functions are labeled with Strouhal numbers, which range from 0.15 to 0.30.

root-mean-square surging u_e/U_e in the exit plane at four Strouhal numbers: St = 0.15, 0.20, 0.25, and 0.30, the accessory experimental conditions being listed in table 3. As the Strouhal number rises from 0.15 to 0.30, the response at each level of forcing rises progressively. Within the range of small u_e/U_e where the fundamental (not shown) depends linearly on forcing, the slope du/du_e rises monotonically in accord with stability theory. The amplitude u/U_e at which nonlinear saturation begins to set in rises as well.

Figure 17 illustrates the consequences of forcing at higher Strouhal numbers. The amplitude response at St = 0.30 appears once again, together with response functions at St = 0.35, 0.40, 0.45, and 0.50, each measured on the centerline at x/D = 4. The slope du/du_e continues to rise monotonically with Strouhal number in the linear region near $u_e/U_e = 0$, but nonlinearity imposes an increasingly powerful restraint on the maximum attainable response. The saturation limit of u/U_e *decreases* continuously as the Strouhal number increases from 0.30 to 0.50. *The mode having a Strouhal number of 0.30 is preferred in the sense that it can attain the highest possible amplitude under the combined effects of linear amplification and nonlinear saturation.*

We measured response functions at St = 0.55 and 0.60, but they fall too near the St = 0.50 curve to be plotted in figure 17. The maximum attainable response becomes very nearly constant at $u/U_e \approx 10\%$ for the *highest* Strouhal numbers we investigated. That result accords with an observation of Freymuth (1966), that waves on a free laminar boundary layer tend to saturate at a constant amplitude at the *lowest* Strouhal

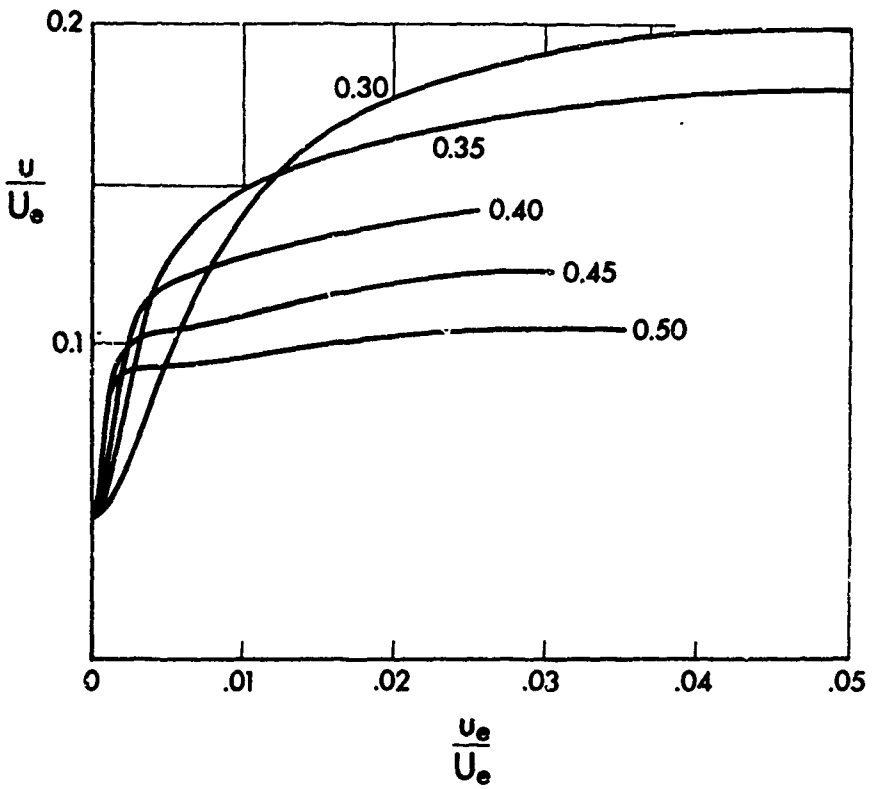

Figure 17. Amplitude-response functions continued through the Strouhal-number interval 0.30 to 0.50.

numbers he investigated, which were mostly greater than 3.0 based on jet diameter, and never below 0.9. It therefore seems likely that u/U_e = 10% persists as the upper limit of response at x/D = 4 for Strouhal numbers ranging from 0.5 up to values so high that the thickness of the laminar boundary layer, if any, becomes involved.

The curves in figures 16 and 17 can be regarded as cuts through an amplitude-response *surface* above the plane of forcing parameters (St, u_e/U_e). Figure 18 is a contour map of the response surface, constructed from the original response curves and their cross-plots against St. The abscissa of figure 18 is the Strouhal number St, the ordinate is the forcing amplitude u_e/U_e, and the contours are levels of constant response u/U_e measured on the centerline at x/D = 4. The higher contours point like daggers to the Strouhal number 0.30. Looking along a cut at a constant and very small u_e/U_e, one would find no Strouhal-number preference. Linear stability theory applies only along such cuts, so its failure to explain the Strouhal-number preference was inevitable. One must look along a horizontal cut at higher u_e/U_e, say u_e/U_e = 1%, to find a mode of maximum amplitude. Note that the Strouhal number of the mode preferred along a horizontal cut decreases somewhat with increasing u_e/U_e. At a forcing amplitude u_e/U_e = 0.5%, the response attains a maximum at St = 0.37. When u_e/U_e = 1%, the maximum occurs at St = 0.34, and the maximum occurs at St = 0.30 exactly, when u_e/U_e = 2%. Thereafter the variation of preferred St with increasing u_e/U_e is slow. The assertion that 0.30 is the preferred Strouhal number must be qualified slightly, because it involves the tacit assumption that the forcing amplitude u_e/U_e

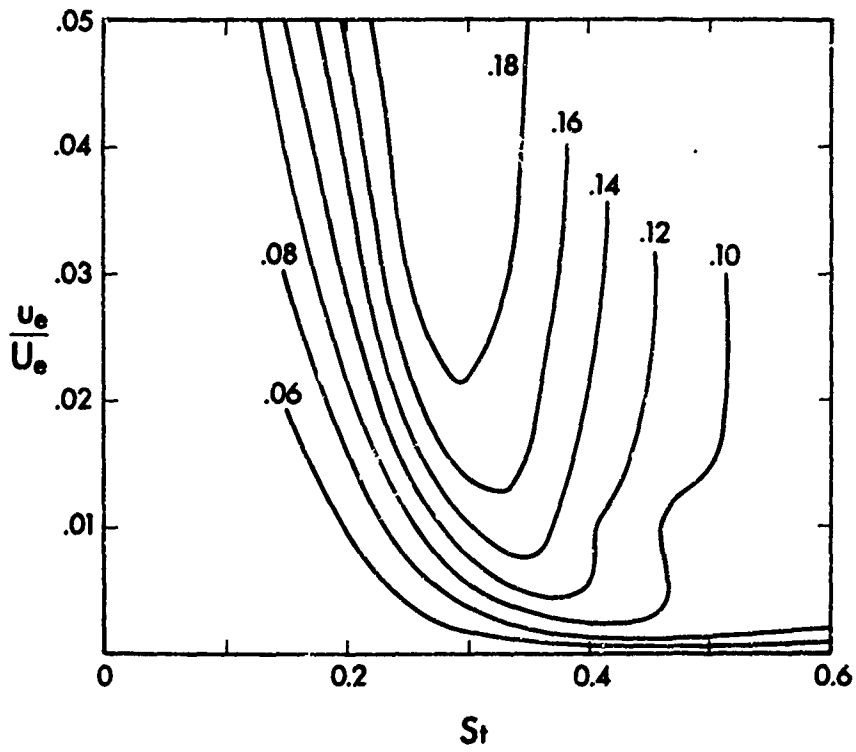

Figure 18. Contour map of the total response four diameters downstream on the centerline, as a function of Strouhal number and amplitude of forcing. The contours are labeled with u/U_e, which rises by 0.02 from one curve to the next. The abscissa is the contour $u/U_e = 0.04$ approximately, the turbulence intensity in the absence of forcing.

is 2% or more. The precise Strouhal-number preference for any given level of forcing can be deduced from figure 18.

Imagine a round jet in a turbulent state having *no* orderly structure of the kind under study. The turbulence excites waves on the jet column just as our exit-plane surging does, except that the turbulent forcing is not confined to one frequency. The turbulence hunts over the (St, u_e/U_e) plane, so to speak, triggering wavetrains at random. Those triggered at a Strouhal number of 0.30 reach an especially high amplitude, sporadically overthrowing the chaos assumed as the initial state of turbulence. The structure of big eddies can be expected to pull in around the mode at St = 0.30, which attains the highest possible amplitude under nonlinear saturation.

6. Axial Profiles at Various Strouhal Numbers

We showed in the foregoing section that the Strouhal number of maximum response at x/D = 4 varies somewhat with u_e/U_e, having no finite value at $u_e/U_e = 0$ and acquiring values around 0.30 for $u_e/U_e \geq 2\%$. As might be expected, the preferred Strouhal number also depends to some extent on x/D. The waves all amplify with distance downstream, so a high x/D corresponds in a loose way to a high u_e/U_e. Here we examine the correspondence by presenting axial profiles of the total response u/U_e for the same Strouhal numbers as in §5, but for a forcing amplitude u_e/U_e fixed at 2%.

Figure 19 shows centerline profiles of response to 2% forcing at the Strouhal numbers 0.15, 0.20, 0.25, and 0.30 (cf. figure 16). The curve

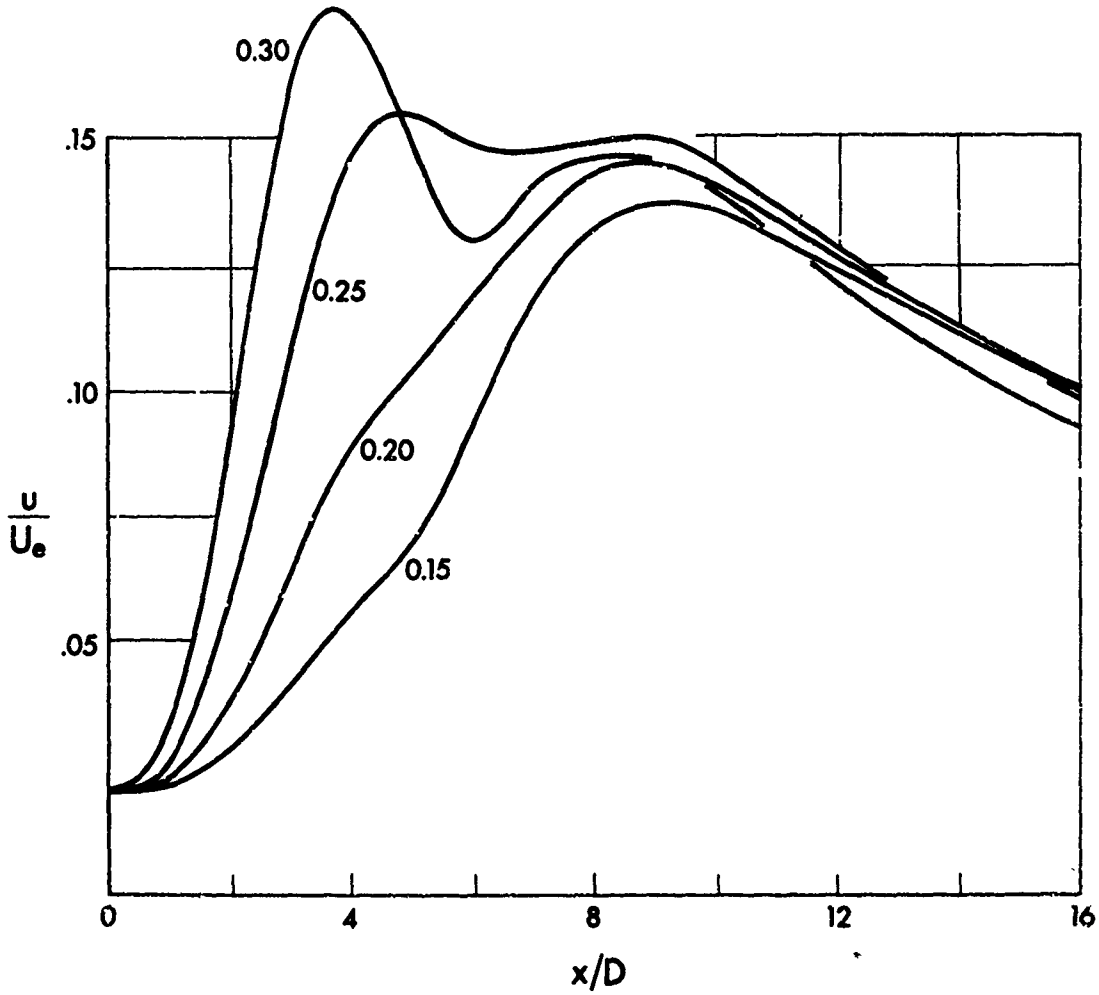

Figure 19. Centerline profiles of turbulence intensity, under 2% forcing in the Strouhal-number interval 0.15 to 0.30. The Strouhal numbers are given on the plot.

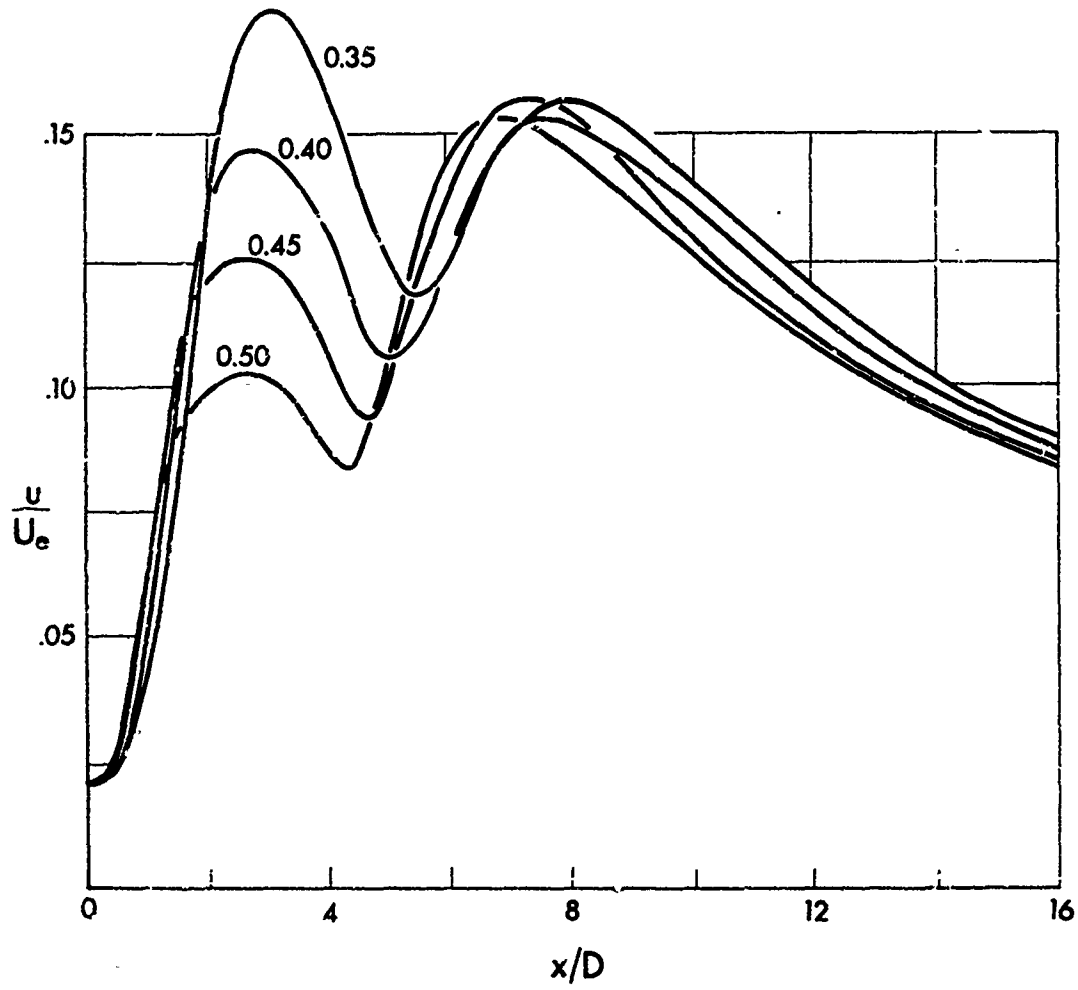

Figure 20. Centerline profiles continued through the Strouhal-number interval 0.35 to 0.50.

pertaining to St = 0.30 has already appeared in figure 13, which shows how the data points were generally spaced. The effect of forcing at St = 0.15 is very slight, and the axial intensity profile nearly coincides with the unforced case in figure 8. As St rises from 0.15 to 0.30, the ramp-like part of the intensity profile bulges upward in the interval x/D = 0 to 5. When St = 0.30, the amplitude of the forced wave attains a sharp maximum around x/D = 4 and then decays downstream into the secondary maximum due to natural turbulence.

Figure 20 shows the primary peak collapsing as the Strouhal number advances through the values 0.35, 0.40, 0.45, and 0.50 (cf. figure 17). At small distances x/D, the spatial growth rate $d(u/U_e)/d(x/D)$ increases monotonically with Strouhal number throughout the range 0.15 to 0.50, as one would expect from linear stability theory. The peak response u/U_e is realized on the St = 0.30 profile, near x/D = 4. The location x/D = 4 was therefore the correct choice for defining the Strouhal-number preference in §5, because the mode of maximum response at x/D = 4 is also the mode of maximum response over all values of the parameters St and x/D.

By analogy with §5, the curves in figures 19 and 20 can be regarded as cuts through a response surface above the (St, x/D) plane. A contour map of the surface is presented in figure 21, which is analogous to figure 18. The contours are again levels of constant response u/U_e, and the abscissa is still the Strouhal number St. The ordinate this time is x/D, the forcing amplitude u_e/U_e being fixed at 2%. The peak within the perimeter u/U_e = 16% defines the Strouhal number of the mode preferred under 2% forcing and the location at which it attains maximum amplitude.

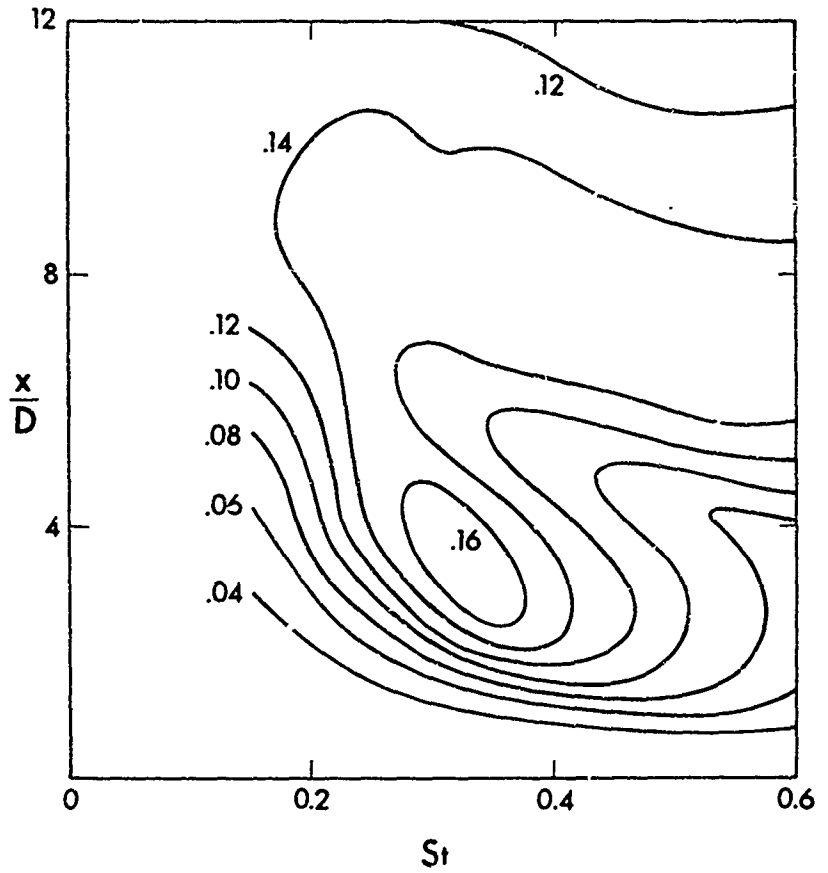

Figure 21. Contours of centerline turbulence intensity as a function of Strouhal number of forcing and distance downstream. The forcing amplitude is fixed at 2%. The contours are labeled with u/U_e, which changes by 0.02 from one curve to the next.

Note that a clear Strouhal-number preference cannot be discerned by looking along a horizontal cut at small x/D. All waves are linear sufficiently close to the nozzle even when driven by a 2% surging, and the higher the Strouhal number in the linear regime, the greater the rate of spatial amplification.

Axial profiles at St = 0.60 were also measured and deserve special comment. Figure 22 is a plot of the root-mean-square centerline response u/U_e measured under the conditions u_e/U_e = 2% and St = 0.60, twice the Strouhal number of the preferred mode. The curve without data points is the intensity profile for the unforced case, taken from figure 8. The response profile at St = 0.60 has two curious attributes: an abrupt change of slope at x/D = 4, and a shift of the background-turbulence profile a full three diameters upstream toward the nozzle. The corresponding profile of mean centerline speed U/U_e is plotted in figure 23, which confirms the powerful effect of forcing at St = 0.60. The potential core has shortened by two diameters, and the asymptotic decay profile has drawn inward three diameters. The mean-speed profile may be compared with figure 15, which shows the more moderate changes produced by driving the preferred mode directly. The virtual origin of the decay profile shifts only two diameters upstream, as explained in §4.

Judged solely on the basis of figures 22 and 23, the consequences of driving the jet at a Strouhal number of 0.60 seem paradoxical: the mode saturates at a relatively modest amplitude, say u/U_e = 7.5%, yet deforms the jet more powerfully than the preferred mode having more than twice the saturation amplitude. The resolution of the paradox was apparent from

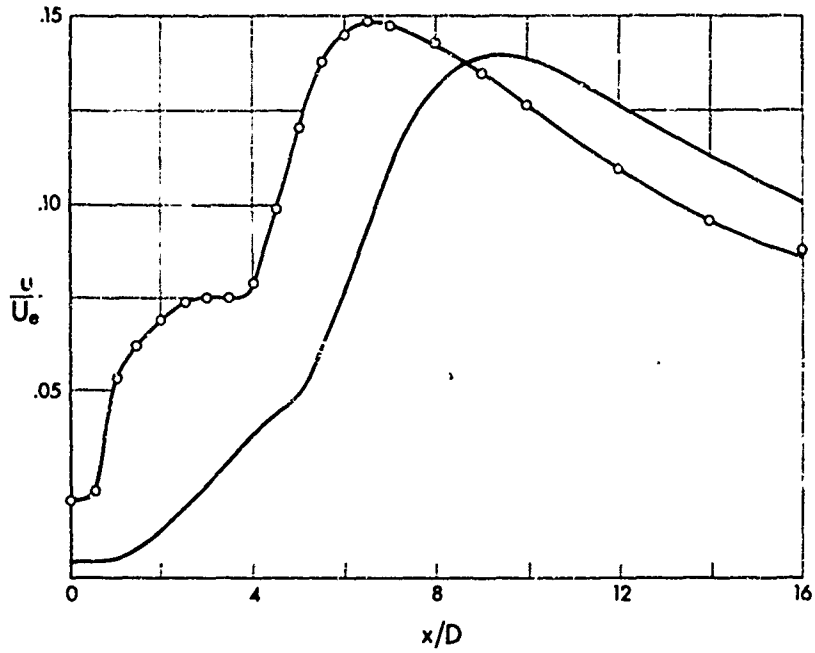

Figure 22. Centerline profile of turbulence intensity under 2% forcing at a Strouhal number of 0.60. The curve without data points represents the unforced case and is taken from figure 8.

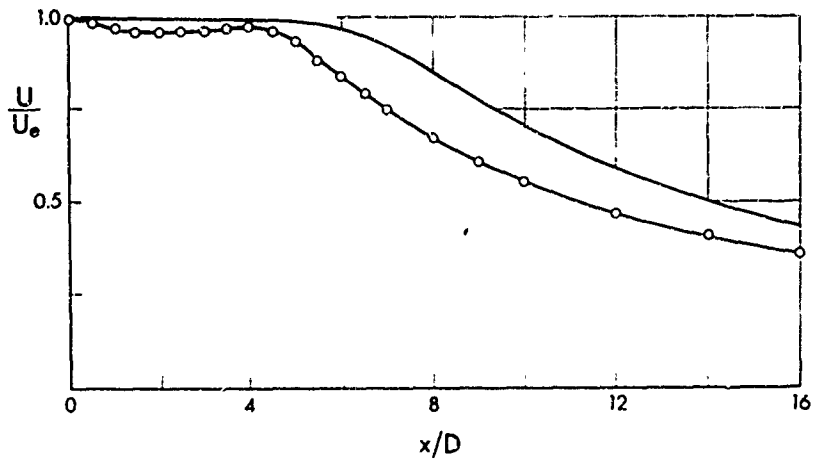

Figure 23. Mean-speed decay along the centerline under 2% forcing at a Strouhal number of 0.60. The curve without data points is the unforced profile taken from figure 7.

oscilloscope traces of the hot-wire signal: the St = 0.60 mode survives only up to x/D = 4, at which point a violent St = 0.30 subharmonic arises, presumably by the process of engulfment seen in figure 6(a). The changes in the jet are not wrought by the St = 0.60 mode directly, but instead by its subharmonic at the preferred Strouhal number of 0.30. The St = 0.60 fundamental merely serves as an amplifier between the 2% surging in the exit plane and the 7.5% surging downstream at the point of subharmonic formation.

7. Summary Description of the Modes

In the two previous sections we studied the response u/U_e, first by setting x/D = 4 and allowing u_e/U_e and St to vary, and then by setting u_e/U_e = 2% and allowing x/D and St to vary. Here we bring the response study to its logical completion by setting St = 0.30 and varying u_e/U_e and x/D. The reason for doing so is that the other procedures have left open questions about the eventual decay of orderly structure. Why do the intensities in figures 19 and 20 decay beyond the primary peaks? What effect does the damping have on the choice of a preferred mode? The nature of the problem can best be judged from figure 14, which shows the evolution of fundamental and harmonic amplitudes under the forcing conditions St = 0.30, u_e/U_e = 2%. The growth of the fundamental is caused by linear instability, and the peak amplitude is determined mainly by nonlinear saturation. The nature of the decay from x/D = 4 to 8 remains to be studied, together with its effect on the precise location and

amplitude of the peak.

Figure 14 conveys the impression that the fundamental $u_{0.30}/U_e$ would peak at some x/D and thereafter decay, even if the mode were forced so slightly that nonlinear saturation never took hold. At least two linear decay mechanisms are available. One possibility is that fine-scale background turbulence acts as an eddy viscosity and grinds the wave down. A second and less conjectural possibility is that the wave, as it propagates downstream, encounters mean velocity profiles which are progressively more stable with respect to axisymmetric disturbances. All axisymmetric modes amplify on a top-hat velocity profile, but all decay on a bell-shaped profile of the kind a turbulent jet assumes downstream of the potential core (Batchelor & Gill 1962). An axisymmetric mode could be expected to grow around the potential core, then lose its grip on the mean field in the transition region and die away. A similar mechanism terminates the growth of waves on a spreading two-dimensional laminar wake (Ko, Kubota & Lees 1970).

Figure 24 shows centerline profiles of the fundamental $u_{0.30}/U_e$ driven at a Strouhal number of 0.30. The lowest curve represents the case $u_e/U_e = 0$ and is included to show the root-mean-square background fluctuations admitted through the finite filter window. The remaining profiles are associated with the forcing amplitudes u_e/U_e = 0.25%, 0.5%, 1%, 2%, and 4%, doubling from one value to the next. The profile for u_e/U_e = 2% is based on the same data as figure 14. The profiles here are plotted in semi-logarithmic coordinates to distinguish linear and nonlinear mechanisms. If the jet were a linear system, then the axial

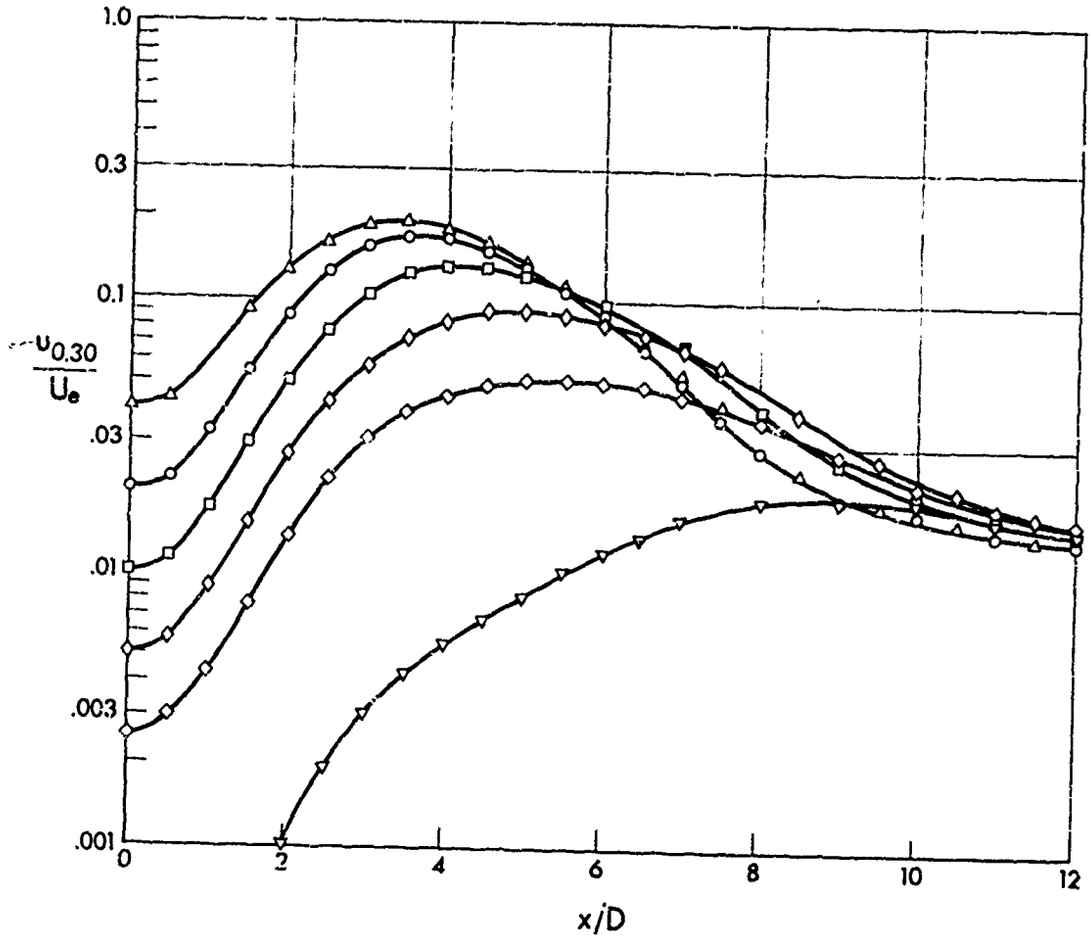

Figure 24. Centerline intensity profiles of the fundamental wave driven at a Strouhal number of 0.30. The data symbols denote the following forcing amplitudes u_e/U_e: ▽ no forcing, ◇ 0.25% forcing, ◇ 0.5%, □ 1%, ○ 2%, and △ 4%. The ordinate $u_{0.30}/U_e$ is logarithmic, so the forced profiles would have had the same shape had the jet been linear.

response profiles would have the same shape regardless of forcing amplitude, which would merely locate each profile along the logarithmic ordinate u/U_e. Indeed the axial intensity profiles for the two lowest forcing levels, u_e/U_e = 0.25% and 0.5%, differ only by a constant vertical displacement out to the region x/D = 6 or 7 where background turbulence takes over. Those profiles show how a forced wave behaves in the absence of nonlinear saturation: the wave grows more-or-less exponentially with distance downstream, grows less rapidly near the tip of the potential core, reaches a peak proportional to forcing amplitude at x/D = 5.5, and thereafter decays under the action of a changing mean field or eddy damping. The total amplification u/u_e at x/D = 5.5 is about 18.

At higher levels of forcing, the jet behaves as a linear system only within the first diameter or two of the exit. The peak of the u_e/U_e = 1% profile is only 47% higher than the peak of the u_e/U_e = 0.5% profile. The fractional increase of the peak intensity drops to 27% as u_e/U_e doubles from 1% to 2%, and to 14% under the final doubling. The main effect of increasing the root-mean-square surging beyond 1% is to draw the point at which the wave saturates inward toward the nozzle. At a forcing amplitude of 0.25%, the fundamental amplitude $u_{0.30}/U_e$ peaks at x/D = 5.5, which is therefore the point where the linear mechanisms of growth and decay just balance. At a forcing level of 1%, the peak occurs at x/D = 4.2, and it drops to x/D = 3.4 when the forcing level reaches 4%. Notice how the curves associated with the two highest levels of forcing, u_e/U_e = 2% and 4%, knit together into a common decay profile after saturating.

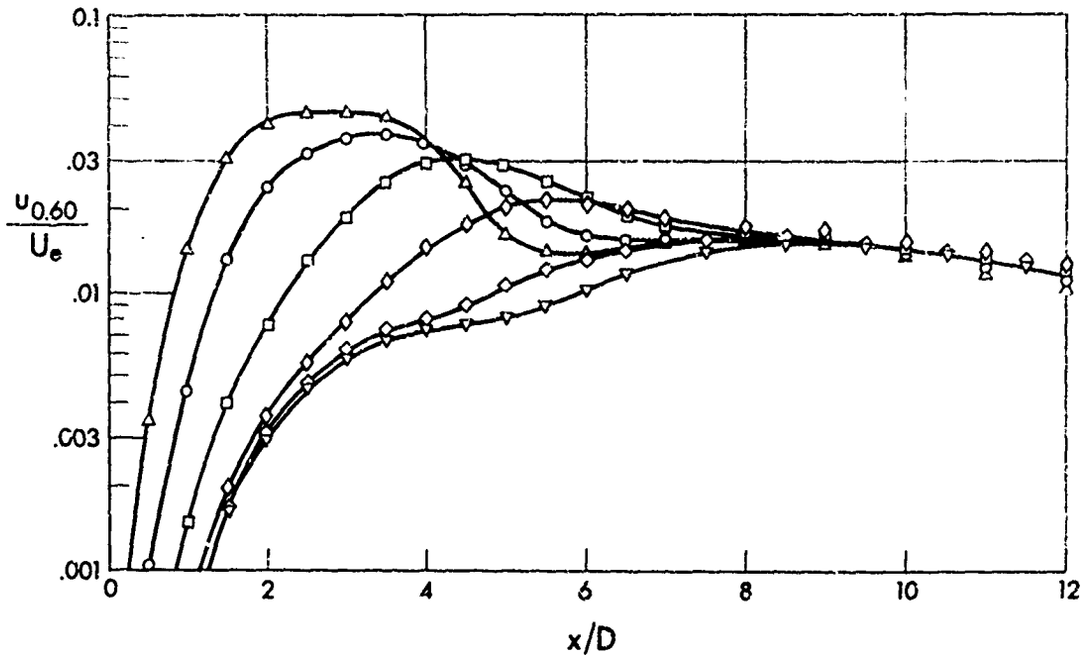

Figure 25. Centerline profiles of the harmonics associated with the fundamentals of figure 24. The Strouhal number of forcing is 0.30, and the data symbols denote the same forcing amplitudes as in the previous figure. The ordinate $u_{0.60}/U_e$ is again logarithmic.

Figure 25 is a semi-logarithmic plot of the harmonic $u_{0.60}/U_e$ under the six forcing conditions of figure 24: the lowest curve is the filter-window background, and the other five are harmonic profiles under forcing amplitudes u_e/U_e that double sequentially from 0.25% to 4%. Again the data for u_e/U_e = 2% are taken from figure 14. The harmonic profiles have the character one would expect from the associated fundamentals. Forcing at u_e/U_e = 0.5% or below evokes only a slight harmonic response, which is why the fundamental is free of nonlinear saturation in that range. As the forcing level increases beyond 1%, a stronger and stronger harmonic arises to inhibit the growth of the fundamental. Raising the forcing amplitude from 2% to 4% brings the harmonic forth at a smaller x/D but does not greatly enhance its amplitude.

Figures 24 and 25 pertain to the St = 0.30 mode, but the qualitative understanding we have drawn from them is general: a forced axisymmetric wave amplifies owing to the linear instability of a top-hat jet column, saturates under the nonlinear action of a harmonic, and finally decays owing to an essentially linear process, either mean-field changes or eddy damping.

Having reached an understanding from the hot-wire data, we returned to flow-visualization experiments for confirmation. The changes made since the photographs of §2 were taken should be recalled: figures 4 and 6 show a 1-inch jet with a laminar boundary layer and without artificial surging, whereas the forced jet has a diameter of 2 inches and a fully turbulent boundary layer. Because the volume flow quadrupled at the transition from a 1-inch to a 2-inch jet, we could not retain fog as a

means of visualization. Boundary-layer turbulence and higher Reynolds numbers put the schlieren method to even greater disadvantage than before, but schlieren photography was the only option. Happily the effects of forcing are spectacular enough to show through fine boundary-layer turbulence.

Three of the schlieren photographs are presented in figure 26. They were taken much the same way as those of figure 4, except that Type 52 Polaroid film of moderate contrast was used to suppress irrelevant detail. Photography under forced conditions required special care, because the introduction of CO_2 causes the resonance frequencies of the plenum to shift slightly. If the loudspeaker were tuned in the absence of CO_2, then u_e/U_e would fall off the resonance peak when CO_2 was introduced. The problem was easily circumvented by tuning the system while maintaining a flow of CO_2 appropriate for photography. The 185 Hz resonance of table 3, for example, shifted to 181.4 Hz, which was used as the frequency for driving the St = 0.30 mode. The shaft entering from the right in figures 26(b) and (c) is the hot-wire probe, located at x/D = 4 and left in the flow to monitor the tuning.

Figure 26(a) shows the 2-inch CO_2-seeded jet without forcing. The usual hints of orderly structure appear, with the usual ambiguity (cf. figure 1). Figures 26(a) and (b) were taken at the same Reynolds number, Re = 106,000, but the flow seen in 26(b) was forced under the conditions St = 0.30, u_e/U_e = 2%. Figure 26(c) was taken under the forcing conditions St = 0.60, u_e/U_e = 2%. Figures 26(b) and (c) illustrate the kinematics of forced waves in a striking manner. The St = 0.60 mode

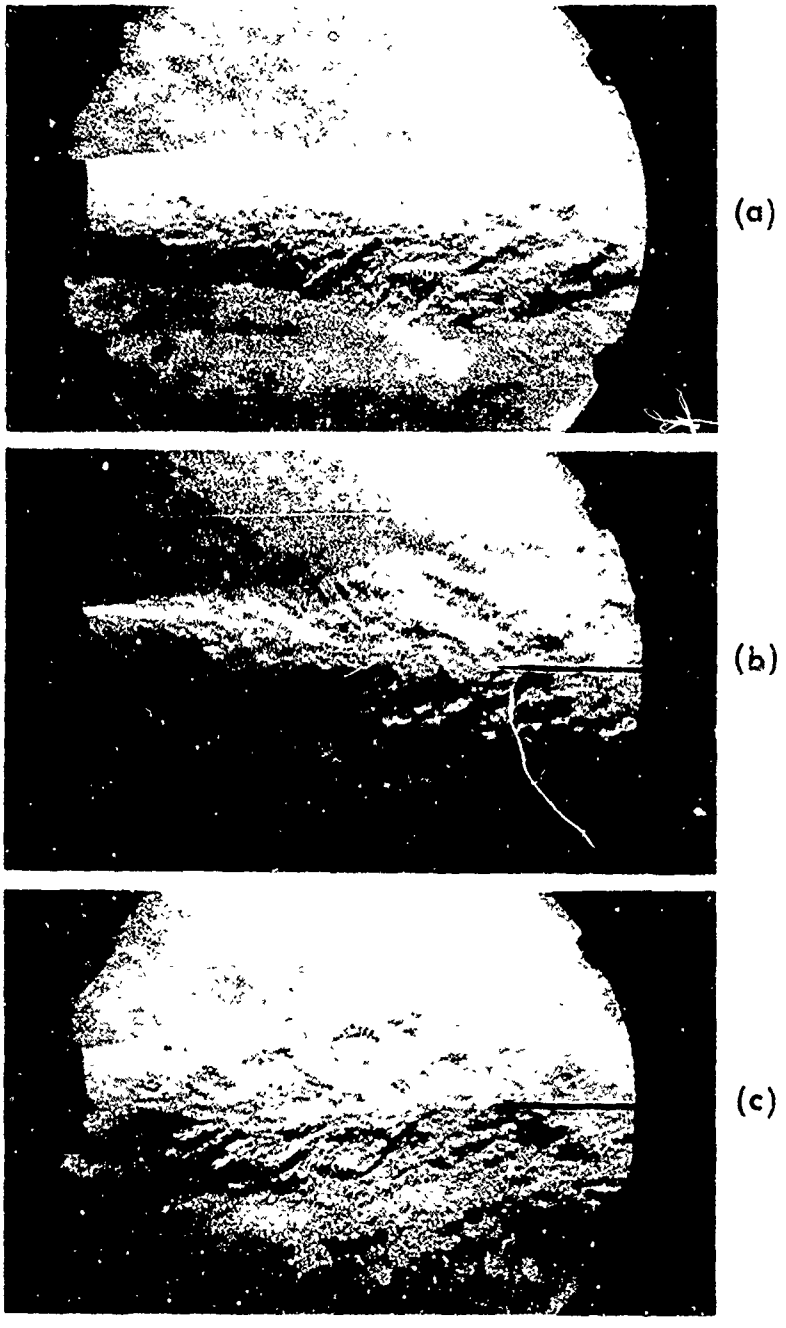

Figure 26. Schlieren photographs of the 2-inch jet seeded with CO_2. Part (a) shows the unforced jet at an exit speed of 103 ft/sec and a Reynolds number of 106,000. The remaining parts show the jet under 2% forcing at Strouhal numbers of (b) 0.30 and (c) 0.60.

grows quickly near the nozzle but saturates 1-2 diameters downstream, in accord with the measured intensity profile of figure 22. A train of three saturated waves propagates toward x/D = 4 and there suffers a violent transformation, leading to the enormous spreading angle evident in figure 26(c). The St = 0.60 mode contorts the surface of the jet column into steep waves but cannot penetrate deep enough to disintegrate the column as a whole. The St = 0.30 mode shown in figure 26(b) grows more gradually downstream of the nozzle but eventually causes contortions as steep as those of the St = 0.60 mode. Because of its greater wavelength, the St = 0.30 mode penetrates deep into the jet column and causes its virtual disintegration.

8. Influence of Forcing on Entrainment and Background Turbulence

We have concentrated so far on the structure of the forced waves themselves, and now we turn to their effect on the mean flow and on background turbulence. The work presented in this section concerns the St = 0.30 mode alone. It would have been interesting to carry the study of the St = 0.60 mode beyond the centerline profiles of figures 22 and 23, but time fell short.

Figures 27 and 28 display the results of radial hot-wire traverses at five stations along the jet, namely x/D = 0.025, 2, 4, 6, and 8. Part (a) of each figure shows radial profiles in the absence of forcing, and part (b) the corresponding profiles under the forcing conditions u_e/U_e = 2%,

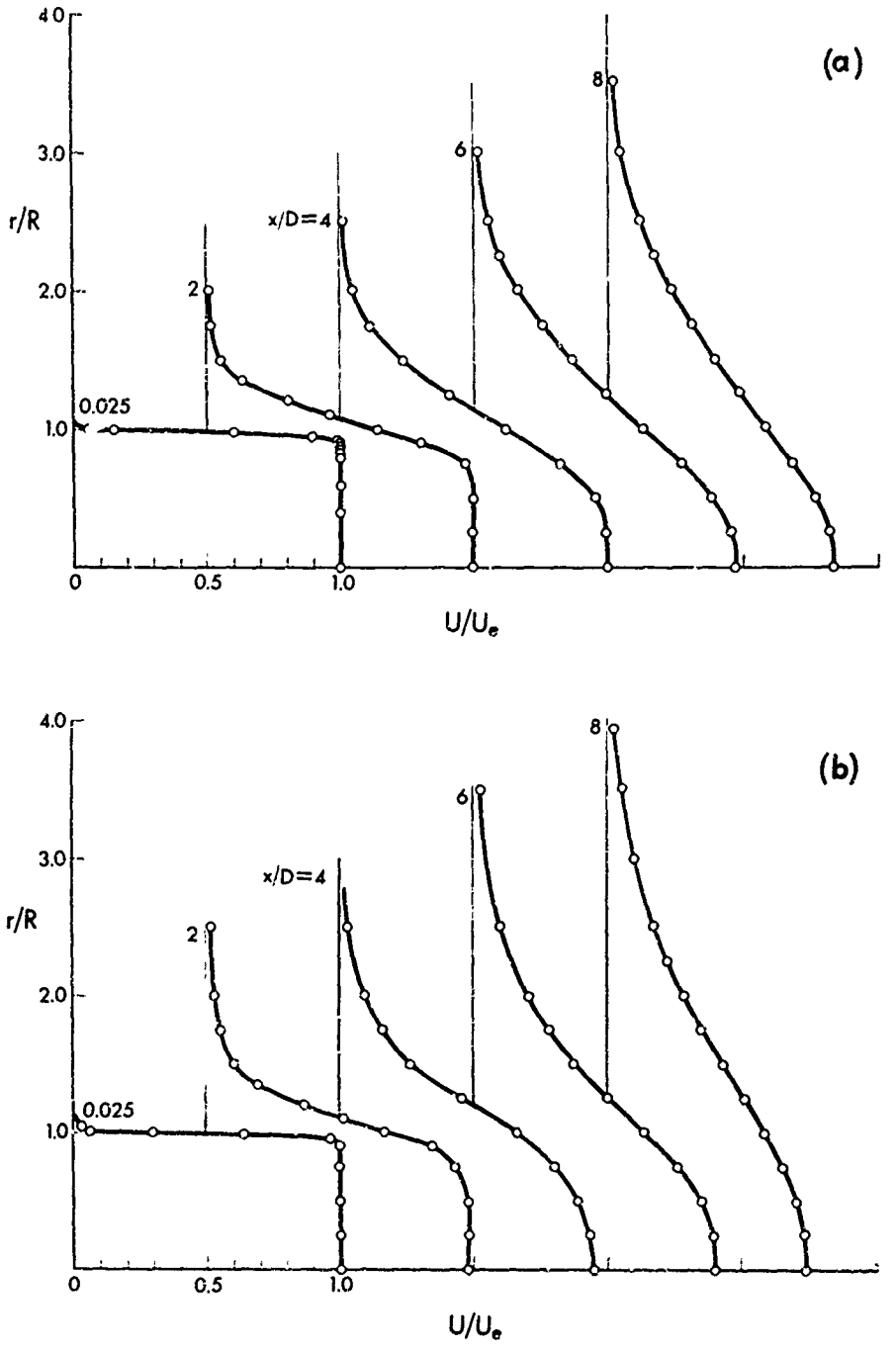

Figure 27. Radial mean-speed profiles at five stations along the jet axis: (a) without forcing, and (b) with 2% forcing at a Strouhal number of 0.30. The stations x/D are specified near the ordinates of the profiles, which are arranged to suggest the spatial structure of the jet.

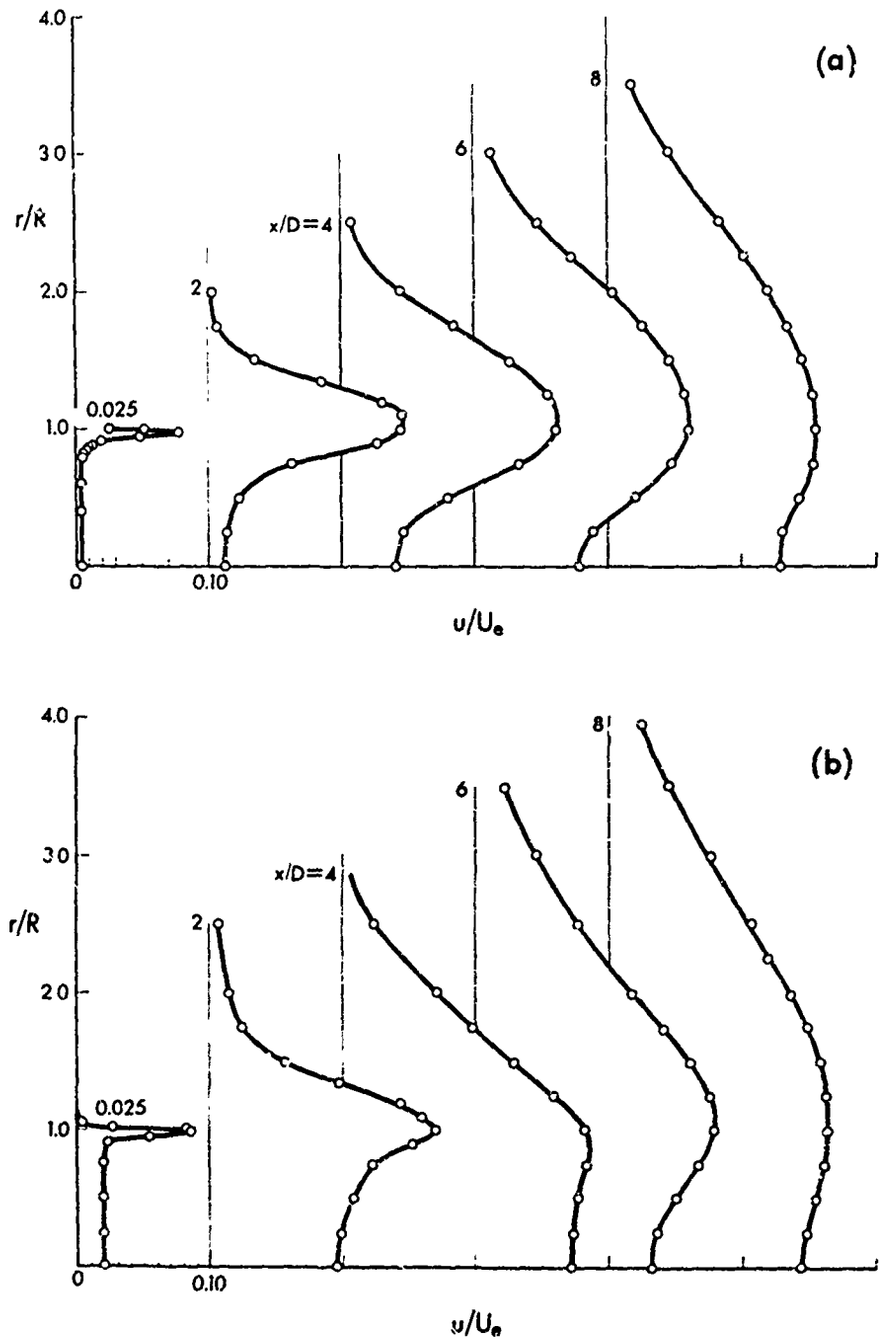

Figure 28. Radial intensity profiles of the axial component of turbulent velocity: (a) unforced, and (b) forced at a level of 2% and a Strouhal number of 0.30.

St = 0.30. Figure 27 shows $U(x,r)/U_e$, the axial component of mean velocity, and figure 28 shows $u(x,r)/U_e$, the root-mean-square axial component of turbulent velocity. The ordinate in each case is r/R, R being the 1-inch radius of the jet. The profiles are staggered along the abscissas to suggest the spatial structure of the jet and global effects of forcing. Note that the axial spacing is compressed by a factor of four relative to the radial.

According to figure 27, forcing makes no dramatic change in the mean field. The mean profile spreads somewhat faster under forcing, so entrainment is enhanced, but the consequences of forcing appear much more clearly in the radial intensity profiles of figure 28. Forcing is seen to inflate the turbulence level out to x/D = 6, especially on the outskirts of the jet and inside the potential core, which can be taken as the cone generated by a straight line running from x/D = 0, r/R = 1 down to x/D = 6, r/R = 0. The turbulence level in the mixing layer around r/R = 1 is not so strongly affected.

The most interesting property of the mean flow is its volume flux, whose derivative with respect to axial location is entrainment. The volume flux Q(x) is defined by an area integral over the axial component of mean velocity:

$$Q(x) = \int_0^\infty U_i\ (x,r)\ 2\pi r\ dr \quad .$$

The subscript i directs attention to the fact that volume flux makes sense only when one has in mind inner and outer solutions of a comprehensive

velocity field. The notions of volume flux and entrainment are creatures of theory, in the case of a jet, rather than experiment. In order to appreciate that important but subtle point, suppose that an expression is known for the mean axial flow $U_i(x,r)$ within the turbulent region of a jet. Then the volume flux Q can be calculated at each station x, *provided the radial integration of rU_i converges.* The local entrainment is dQ/dx, which means that the jet induces an external potential flow as though it were a line sink of strength dQ/dx. One can show on the basis of similarity arguments that dQ/dx must approach a constant value $k\ Q_e/D$ far downstream, where Q_e is the volume flux out the exit and k is a dimensionless constant (cf. Wygnanski 1964). As a result, the axial component of induced potential flow, say $U_o(x,r)$, approaches $k\ Q_e/4\pi Dr$ at great distances r from the jet axis. The quantity rU_o does not fall to zero as r approaches infinity, and the *volume flux in the induced potential flow is infinite.* The flux Q therefore cannot be defined in terms of the net flow $U = U_i + U_o$, but only in terms of the inner rotational part U_i.

The quantity measured experimentally is U, so a somewhat arbitrary judgment must be made to isolate U_i. The judgment was not very difficult in practice. We replotted the data of figure 27 and others downstream in the form of dimensionless flux profiles $(r/R)\ U(x,r)/U_e$. The potential tails of the flux profiles were obvious, and we simply faired the curves to zero before performing planimeter integrations. Hopefully the faired profiles were good representations of $(r/R)\ U_i(x,r)/U_e$, which could perhaps be measured objectively by conditioning the velocity mean on the presence of turbulence.

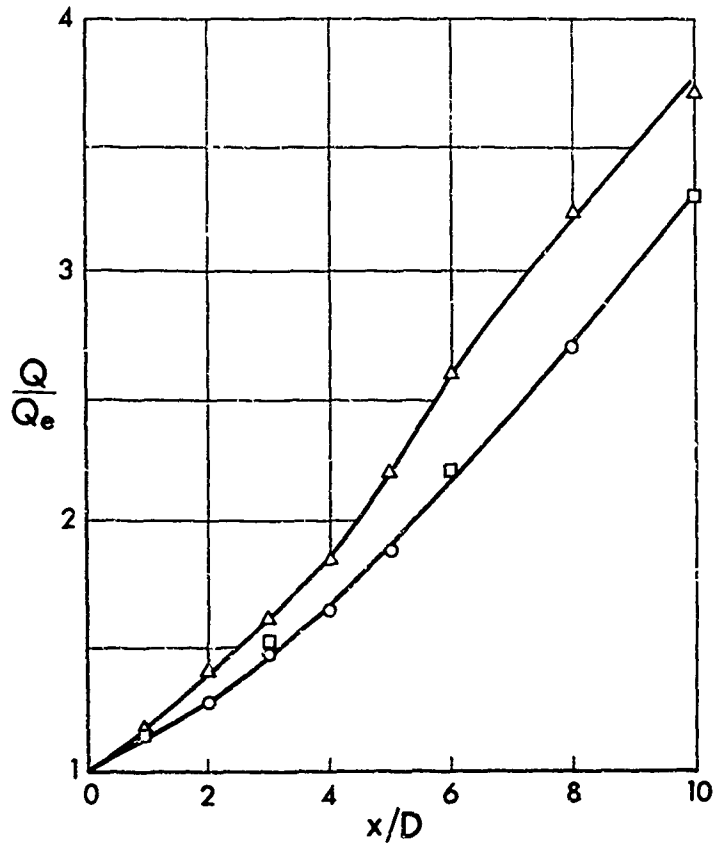

Figure 29. Axial profiles of volume flux, normalized on the flux out the jet exit. The round data symbols denote the unforced case, and the square symbols represent comparable data from Sami *et al* (1967). The triangular symbols denote the case of 2% forcing at a Strouhal number of 0.30.

The resulting normalized flux profiles Q/Q_e are presented in figure 29. The circular data points represent the unforced jet, and the triangular points represent the jet under the forcing conditions $u_e/U_e = 2\%$, St = 0.30. The square points were obtained by integrating the velocity profiles published by Sami, Carmody & Rouse (1967), the same standard being used for fairing the outer part of their curves as for ours. The agreement between their data and our own for the unforced jet is impressive, especially since their Reynolds number was 220,000.

In the absence of forcing, the volume-flux profile is seen to be linear for x/D both large and small, with slopes

$$\frac{dQ}{dx} = \begin{cases} 0.136\ Q_e/D & (x/D \lesssim 2) \quad , \\ \\ 0.292\ Q_e/D & (x/D \gtrsim 6) \quad , \end{cases}$$

measured from figure 29. The entrainment dQ/dx is therefore constant both near to and far from the jet exit, in accord with similarity arguments (Wygnanski 1964). Wygnanski cited figures implying that $dQ/dx = 0.128\ Q_e/D$ in the mixing-layer region near the jet and $0.456\ Q_e/D$ far downstream. The latter value is much higher than we measure and is found to result from an assumed functional form of U(x,r) inappropriate for calculating volume flux. To make sure of the downstream limit, we calculated the volume flux of the asymptotic jet profile measured by Wygnanski & Fiedler (1969), with the result that $dQ/dx = 0.263\ Q_e/D$. The constant is only 10% short of the value 0.292 measured from figure 29 and is probably more reliable, because

Wygnanski & Fiedler took pains to mitigate room drafts. The entrainment rates $dQ/dx = 0.13\ Q_e/D$ near the exit and $0.27\ Q_e/D$ far downstream should both be accurate to within $\pm 0.01\ Q_e/D$.

Forcing under the conditions $u_e/U_e = 2\%$, St = 0.30 is seen from figure 29 to enhance entrainment in the interval x/D = 0 to 6 and particularly in the last two diameters of that interval, beyond the point x/D = 4 where the vortex puffs attain their maximum intensity. Further downstream the volume-flux profile attains the same slope as the unforced case, the virtual origin having been drawn upstream about two diameters. The shift of virtual origin was discussed in connection with figure 15 and can now be understood as the result of enhanced entrainment in the interval x/D = 4 to 6.

We now take up the second topic of this section — the influence of forcing on background turbulence, which means any fluctuations not bound into the driven fundamental or its harmonics. Periodic forcing might reasonably be expected to suppress the larger scales of background turbulence, because big eddies would tend to become locked into the forcing frequency. The simplest statistical quantity bearing on that conjecture is F(f), the spectrum of axial velocity fluctuations at a fixed point (x,r). In the unlikely event that forcing bound up *all* background turbulence, then F(f) would comprise a sequence of spikes at the forcing frequency and its harmonics. If forcing had *no* effect on the background, then F(f) would consist of spikes superposed on a broad-band component identical to the spectrum that exists in the absence of forcing. The measured spectrum should lie between the extremes.

An on-line computer determined the spectra by means of fast Fourier transformation (Pao, Hansen & MacGregor 1969). The program uses the raw linearized hot-wire signal for computing the mean and a high-pass filtered version for computing fluctuation quantities; filtering trims off the direct current to improve resolution. The window of the Krohn-Hite Model 330 band-pass filter lay between 0.2 Hz and a high frequency selected to control aliasing. Both the raw and filtered signals were sent through Dynamics Model 7514 amplifiers and shielded coaxial cables to an IBM Model 1827 analogue-to-digital converter and Model 360-44 computer, the transmission system being free of distortion up to 20,000 Hz. The continuous signals were converted to 18,000 samples per second with a resolution of 14 bits plus a sign bit, and the samples were processed in lots of 8192 dictated by the computer memory capacity. Three hundred lots were typically processed to insure convergence, which was monitored through intermediate print-outs. Since only the larger scales of turbulence were of interest, the spectra could be confined below 9000 Hz and in some cases below 1000 Hz. Spectral windows of 0.078 Hz and 0.24 Hz were used to resolve the forcing frequency and its first two harmonics, and the results were overlapped with broad-band spectra obtained with a 2.18 Hz window. Each time a spectrum was measured, the root-mean-square fluctuation u was obtained both from the spectrum and by the usual analogue method. The results always agreed within ±2%. Analogue checks of several spectral points fell within ±10% of the digital values.

Six spectra are presented in figure 30. Each was measured at the axial station $x/D = 4$, and parts (a), (b), and (c) of the figure correspond

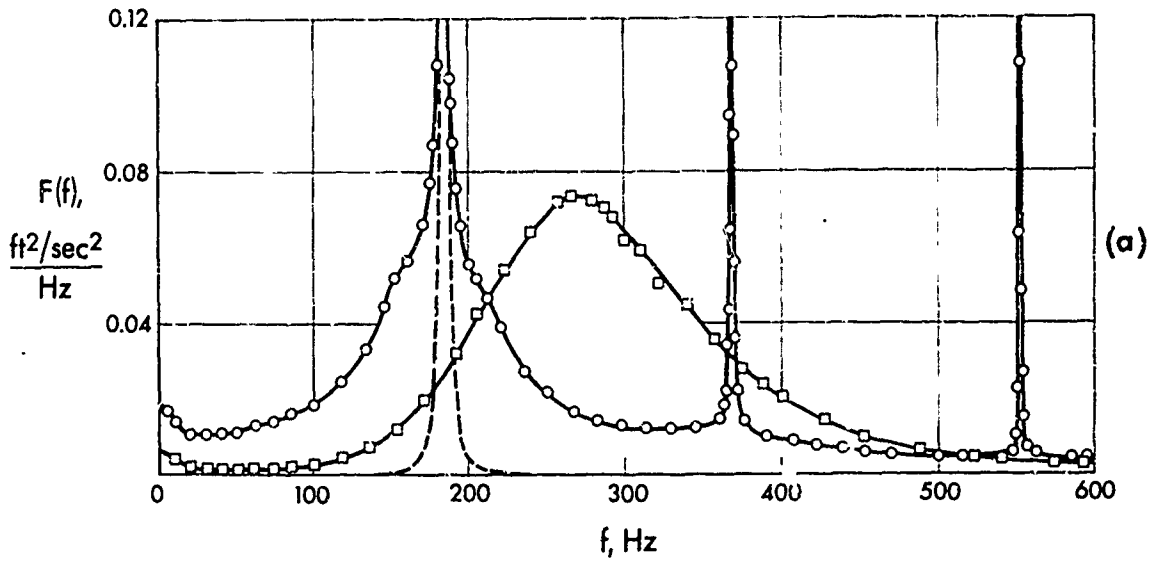

Figure 30. Turbulence spectra at x/D = 4 and (a) r/R = 0, (b) r/R = 1.0, and (c) r/R = 1.5. The square data symbols denote the unforced case, and the round symbols denote the case of 2% forcing at a Strouhal number of 0.30. The computer evaluated many more data than are shown. The dashed spike in part (a) represents a pure sine wave with the power of the fundamental.

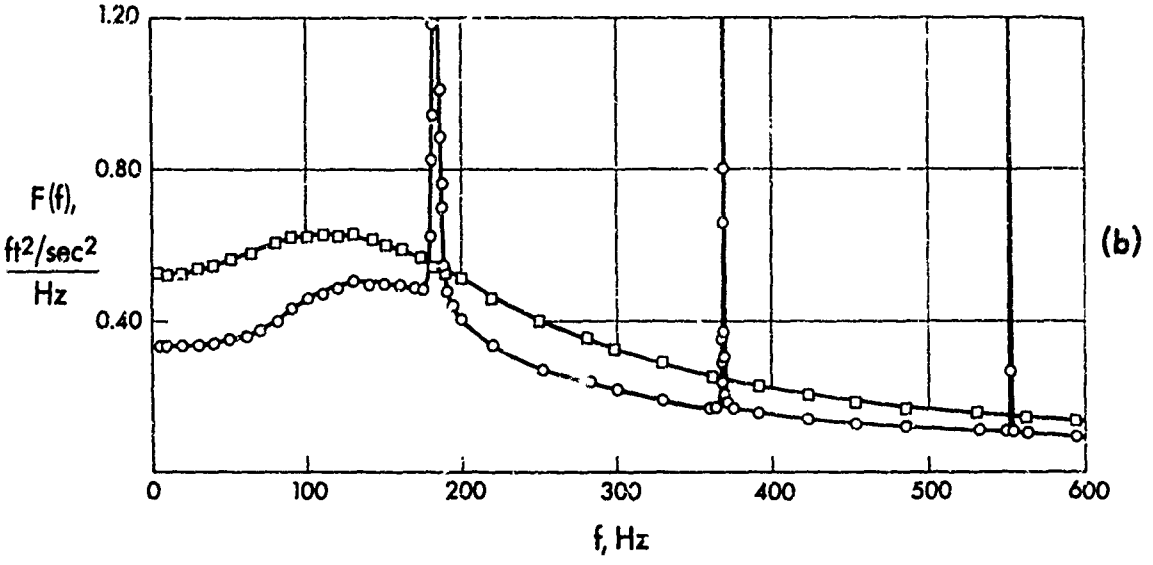
1.20
0.80
0.40
F(f),
ft²/sec²
Hz
0
100
200
300
400
500
600
f, Hz
(b)

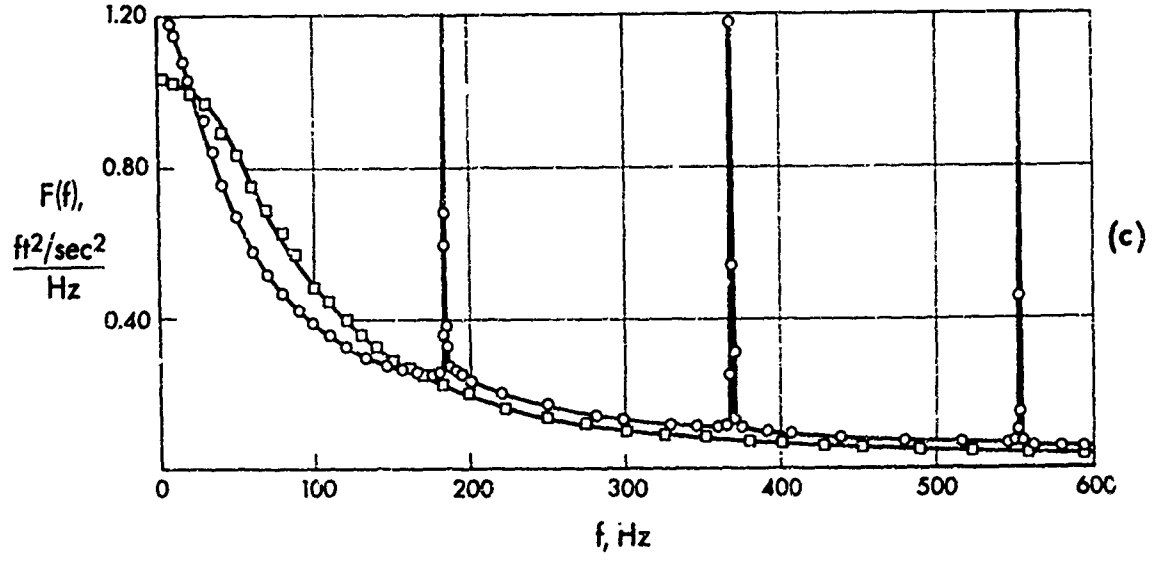
1.20
0.80
0.40
F(f),
ft²/sec²
Hz
0
100
200
300
400
500
600
f, Hz
(c)

to the radial locations r/R = 0, 1.0, and 1.5. The square data points represent the unforced jet, and the round data points show the spectral consequences of forcing under the conditions u_e/U_e = 2%, St = 0.30. The data points are spaced for visual convenience and represent only a fraction of the computer output. The dashed spike in figure 30(a) has the same power content as the turbulence fundamental but was generated by feeding a 185 Hz sine wave through the digital system. The artificial spike is included to show that the digital filter window is narrow compared with the width of the broad-band spectrum underneath.

Each forced spectrum has definite peaks at the forcing frequency 185 Hz and its first two harmonics. For the most part forcing does suppress background turbulence, the exception being at r/R = 1.5 in the frequency interval 20-160 Hz, as shown in figure 30(c). Figure 30(b), obtained with the hot-wire probe at x/D = 4, r/R = 1 in the midst of the mixing layer, shows that the 185 Hz fundamental attracts both higher and lower frequency eddies, though the effect is not so pronounced as one might have wished. Suppression of the background is most evident in figure 30(a), whose ordinate is expanded by a factor of ten relative to the others. Figure 30(a) was obtained with the hot-wire probe at x/D = 4, r/R = 0, just inside the tip of the potential core. Forcing is seen to diminish and gather up the naturally occurring bell-shaped spectrum, almost fixing the phase of the big eddies that leave their signature in the potential core.

With respect to aerodynamic sound production, the important question is whether forcing imposes order on the potential flow *outside* the mixing

region, because a fluctuating exterior potential gives rise to sound. Unfortunately a hot-wire anemometer is useless outside the rotational core of the jet: the steady component of flow is too weak to sweep away the hot-wire wake, and the signal is meaningless. The appropriate measurement could be made outside a high-speed subsonic jet, where the strength of pressure fluctuations would permit the use of a microphone in the near field. We hope such an experiment will be taken up in the future.

9. Comparison with Stability Theory

The reader may have noticed the omission of one easily measured property of the forced waves, namely their lengths. Wavelength measurements have been deferred to this section so that they could be set into a theoretical framework. They have some surprising implications for the stability theory of waves on a jet column.

In order to compare theory and experiment, we suppose that the instantaneous axial component $u^*(x,t)$ of velocity on the centerline has the form

$$u^* = u_1^* e^{ax} \cos k(x-ct) \quad .$$

k is the wavenumber, a the spatial amplification rate, and c the phase velocity of the forced wave, all three parameters being real. The wavelength λ is defined as the distance between every other zero intercept of u^*, or as the distance between consecutive peaks. The two definitions

give the same length λ, related to k by the formula $k = 2\pi/\lambda$. The phase velocity c equals $f\lambda$, f being the known forcing frequency. The amplification rate a can be taken as proportional to the slope of the straight segment of a semi-logarithmic amplitude profile like those of figure 24. Admittedly the straight intervals are not extensive, and one could question whether exponential growth occurs anywhere. The profiles curve upward just downstream of the exit, probably because the uniform surging in the exit plane relaxes into the shape of a linear eigenmode. The profiles curve downward beyond x/D = 3 as the jet ceases to resemble a uniform column. Within a restricted interval, however, the forced mode may behave like a linear wave on a doubly infinite jet column, and that is the issue which measurements of λ can clarify.

We carried out the measurements by positioning the hot wire on the centerline, noting the location of a wave peak on the screen of an oscilloscope triggered by the loudspeaker input, then translating the hot wire downstream without changing the phase of the trigger, until a new peak coincided with the location of the old. The net translation of the hot wire was the wavelength λ, which is tabulated below for Strouhal numbers St ranging from 0.15 to 0.80:

Table 4. Wavelengths of the forced modes.

St	0.15	0.20	0.25	0.30	0.35	0.40
λ/D	5.75	3.87	3.17	2.38	1.83	1.69
St	0.45	0.50	0.55	0.60	0.70	0.80
λ/D	1.44	1.23	1.13	1.06	0.91	0.81

The signal displayed on the oscilloscope screen was unfiltered, since no filtering was needed for repeatable measurements. The forcing amplitude was chosen at each Strouhal number so that the wave was linear over most of the hot-wire displacement interval, which bracketed the station $x/D = 4$ except in the cases of very long and very short waves. The measured wavelength was found to depend only weakly on the initial position of the hot wire.

The linear stability theory of waves on a uniform jet column was developed by Batchelor & Gill (1962) and extended to compressible flows by Lees & Gold (1966). For purposes of analysis, the wave is conveniently expressed in complex form,

$$u^* = u_1^* \, e^{i(\alpha x - \omega t)} \quad ,$$

where α is the complex wavenumber $\alpha_r + i\alpha_i$, and ω is the complex frequency $\omega_r + i\omega_i$. By solving for velocity potentials within and without the jet column and matching displacements and pressures across its boundary, Batchelor & Gill derived the following eigenvalue equation for axisymmetric waves:

$$\left(\frac{U_e \alpha}{\omega} - 1\right)^2 = \frac{K_0(\alpha R)\ I_0'(\alpha R)}{K_0'(\alpha R)\ I_0(\alpha R)} \quad .$$

U_e is the jet speed and R its radius, in line with the notation of this paper. I_0 and K_0 are modified Bessel's functions of the first and second kinds.

The real and imaginary parts of the eigenvalue equation constitute two relations among the four quantities α_r, α_i, ω_r, ω_i. Before solving the eigenvalue equation, one usually assumes a restriction on the physical nature of the wave, the conventions being that it grows in time but is purely oscillatory in space, $\alpha_i = 0$, or that it grows in space but is purely oscillatory in time, $\omega_i = 0$. The first case, temporal instability, is easier to treat, because the arguments of the Bessel's functions are real and the eigenvalue equation can be solved directly for $\omega_r(\alpha_r)$ and $\omega_i(\alpha_r)$. Batchelor & Gill have carried out that analysis. The second case, spatial instability, is complicated by the fact that the eigenvalue equation cannot be solved analytically for $\omega_r(\alpha_r)$ and $\alpha_i(\alpha_r)$. It is necessary to solve for ω over the complex plane α, determine the locus $\alpha_i(\alpha_r)$ along which $\omega_i = 0$, and finally evaluate $\omega_r(\alpha_r)$ along that locus. We executed that program on an IBM 360-44 computer, in the belief that spatial instability would bear directly on the orderly structure of jet turbulence.

The quantities of physical interest are k, c, and a, which have the forms

$$\left.\begin{aligned} k &= \alpha_r \\ c &= \omega_r/\alpha_r \\ a &= -\alpha_i \end{aligned}\right\} \quad \text{(spatial)}$$

in the case of spatial instability. The temporal case would seem incompatible with experiment, because the hot-wire signal $u^*(x,t)$ is indeed periodic in time but inhomogeneous in space. The definitions of k and c are the same, but the spatial growth rate a is foreign, strictly speaking, to the hypothesis of temporal instability. If temporal growth is assumed to occur locally in coordinates moving with the phase velocity, however, then the temporal growth rate ω_i can be transformed into a spatial growth rate $\omega_i/c = \alpha_r\omega_i/\omega_r$. The result is a temporal-instability model of the forced modes, capable of being compared to experiment through the prescription

$$\left.\begin{aligned} k &= \alpha_r \\ c &= \omega_r/\alpha_r \\ a &= \alpha_r\omega_i/\omega_r \end{aligned}\right\} \quad \text{(temporal)}$$

Of course we believed that temporal instability would be irrelevant, but the belief proved wrong.

The eigenvalue equation cannot be solved in general without numerical work, but the asymptotic forms of Bessel's functions yield analytical solutions in the limits $kR \to 0$ and $kR \to \infty$. The limits are worth studying, because they embody the essential differences between spatial and temporal

instability. Thus, in the limit of short waves as $kR \to \infty$,

$$aR \to \begin{cases} kR - \frac{1}{2} & \text{(temporal)} \\ kR + O(kR)^{-1} & \text{(spatial)} \end{cases},$$

and

$$\frac{c}{U_e} \to \begin{cases} \frac{1}{2} + \frac{1}{4kR} & \text{(temporal)} \\ 1 + \frac{1}{4kR} & \text{(spatial)} \end{cases}.$$

In the limit of long waves as $kR \to 0$,

$$aR \to (kR)^2 \left(-\frac{1}{2} \log \frac{kR}{A}\right)^{1/2} \qquad \text{(temporal or spatial)},$$

and

$$\frac{c}{U_e} \to \begin{cases} 1 + \frac{(kR)^2}{2} \log \frac{kR}{A} & \text{(temporal)} \\ 1 - \frac{(kR)^2}{4} \; 3 \log \frac{kR}{A} + 1 & \text{(spatial)} \end{cases}.$$

where $A = 1.1229$, a constant involved in the asymptotic expansion of K_0. It is immediately apparent from the limits above that the spatial theory and its temporal analogue predict broadly similar values for the

dimensionless growth rate aR, but that the dimensionless phase velocities c/U_e behave very differently. As kR increases from zero, the phase velocity c/U_e of a temporally growing instability decreases from unity and tends toward an asymptote $c/U_e = 1/2$. The phase velocity of a spatially growing instability rises *above* unity and eventually settles back toward an asymptote $c/U_e = 1$. Short spatially growing waves propagate at the centerline speed U_e, while short temporally growing waves propagate at the average of the speeds inside and outside the jet column, which is $U_e/2$.

The dimensionless amplification rate aR and phase velocity c/U_e are plotted against the dimensionless wavenumber kR in figures 31 and 32. The solid curves are the dispersion relations for spatially growing waves. The dashed curves apply to the temporally growing analogue and are taken from the work of Batchelor & Gill (1962). The data points were obtained from table 4 through the relations $k = 2\pi/\lambda$ and $c = f\lambda$ explained earlier in this section.

The theoretical dispersion relations behave as anticipated from the asymptotic formulas. For both spatial and temporal instabilities, the amplification rate aR rises monotonically with wavenumber kR. In accord with the discussion of §5, neither the spatial nor temporal theory singles a mode of maximum growth rate. Figure 31 shows an unexpected consequence of spatial theory, namely a band of highly unstable but very long waves ($\lambda > 14$ D) lying above the main sequence in the (kR, aR) diagram. Those waves correspond to a gross surging of the jet column but are probably

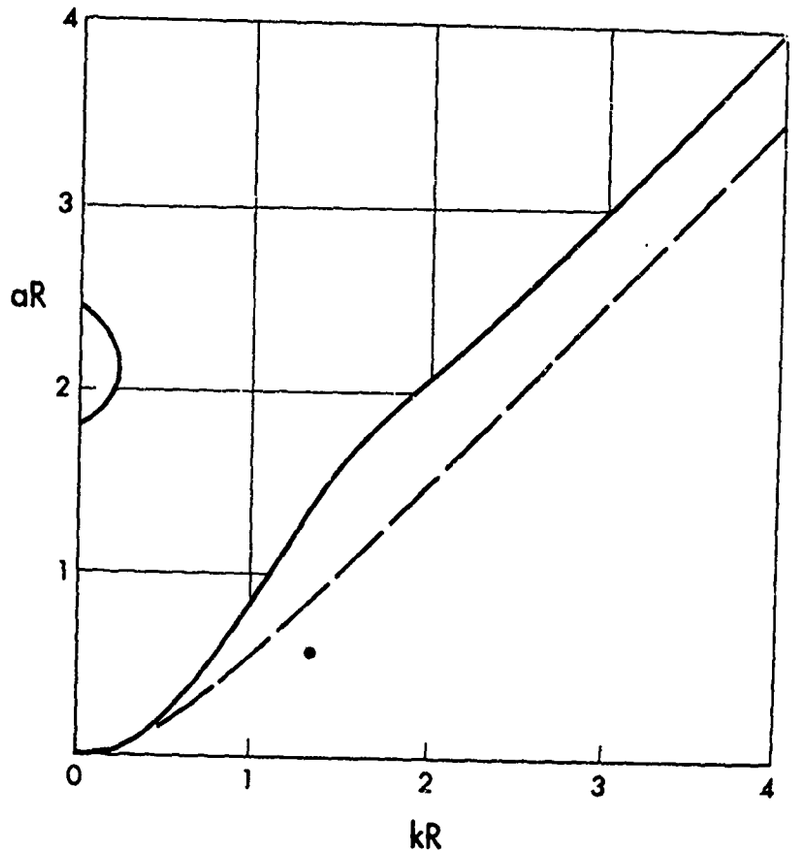

Figure 31. Spatial amplification rate as a function of wavenumber. The solid curves result from the theory of spatially growing waves, and the dashed curve results from a transformation of temporal theory. The experimental datum is the maximum amplification rate of the preferred fundamental, as determined from figure 24.

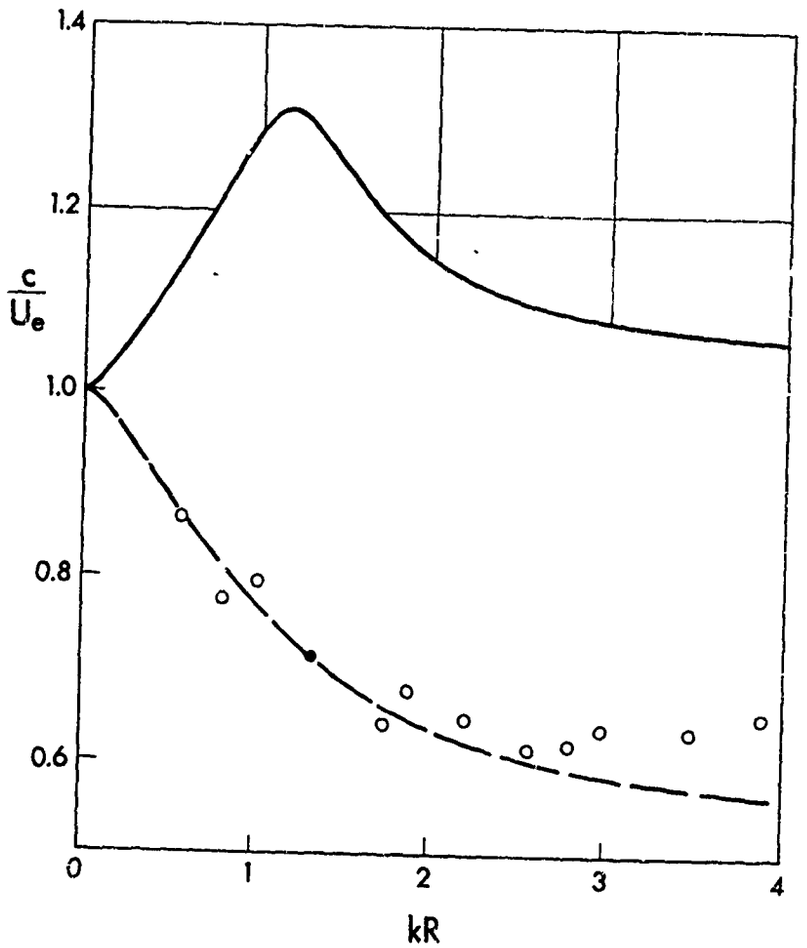

Figure 32. Phase velocity as a function of wavenumber. The solid curve represents spatial theory and the dashed curve temporal. The data are computed from table 4.

too long to have meaning in any physical context. Figure 32 shows that the dimensionless phase velocity c/U_e of temporally growing waves decreases monotonically from 1 to 1/2 as kR increases from 0 to ∞. The phase velocity of spatially growing waves, by contrast, always satisfies the inequality $c/U_e \geq 1$ and reaches a maximum of 1.31 at kR = 1.15.

The surprising aspect of figures 31 and 32 is the relation of the experimental data to the theories. The blank point in each figure denotes the preferred mode, St = 0.30, and is based, in the case of figure 31, upon the maximum slope of the lowest filtered profile in figure 24. No other accurate amplification rates are available. The amplification rate predicted by temporal instability theory is 47% high, and the prediction of spatial theory is much higher. Neither theory predicts the amplification rate at St = 0.30 correctly, but the data plotted in figure 32 do coincide with one of the theoretical dispersion relations $c(kR)/U_e$, *the one corresponding to temporal instability*. The agreement is excellent up to kR = 2.5, beyond which the measured phase velocities lie somewhat above the theoretical. The dispersion relation $c(kR)/U_e$ for spatially growing waves is wholly inconsistent with the data. Plausible as it seems *a priori*, an exponential spatial instability must be ruled out as the mechanism of vortex puffs.

We are faced with a curious anomaly. The temporal instability theory of Batchelor & Gill should be irrelevant to the experimental situation but appears, in an important sense, to be right. Our own spatial instability theory, tailored especially for the experiments, seems to be wrong. The issue is important, because spatial instability theory has lately

come to be regarded as logically superior to temporal theory. Usually the two are compared for slowly growing waves, in which case their predictions are similar. Here the waves grow rapidly, the dispersion relations are distinct, and the data point unambiguously to the temporal instability theory.

The failure of spatial instability theory may be connected with the boundary conditions at downstream infinity. The waves are supposed to diverge exponentially to infinity, but in practice nonlinearity inhibits the divergence. However small the perturbation at $x/D = 0$, the departure of spatial instability theory from a practical flow becomes exponentially large toward downstream infinity. The departure may induce large distortions over the whole field, *even where the original wave is weak enough to be linear*. Because the problem is elliptic, an exponential divergence downstream is inconsistent with linearity everywhere. A temporally unstable wave at least has the merit of being rigorously linear for small times. Apparently it is more advantageous to preserve reasonable boundary conditions than to simulate spatial growth by means of an exponential divergence.

10. Concluding Remarks

An incompressible turbulent jet can sustain orderly modes of axisymmetric flow, including a preferred mode of frequency $f = 0.30\ U_e/D$, wavelength $\lambda = 2.38\ D$, phase velocity $c = 0.71\ U_e$, and maximum rate of spatial amplification $a = 0.58/R$.

The modes obey the dispersion relation c(k) derived by Batchelor & Gill (1962), but nothing in linear stability theory seems to distinguish the mode at $k = 1.32/R$, which attains the highest possible amplitude under nonlinear saturation. Indeed the preference is lost at sufficiently low amplitudes of forcing, according to the contour maps of figures 18 and 21. The prefe.ence arises outside the scope of linear theory, yet linear theory should not be irrelevant. The hot-wire signal of figure 11 is nearly sinusoidal even at the highest forcing amplitude, and the harmonic plotted in figure 12 saturates at only one-fifth the amplitude of the fundamental.

Batchelor & Gill's eigenvalue equation contains a hint of the connection between linear stability theory and the nonlinear selection mechanism. The real limits presented in §9 were taken from the following complex limits of the eigenvalue equation:

$$\left(\frac{U_e \alpha}{\omega} - 1\right)^2 \to \begin{cases} -1 + (\alpha R)^{-1} & \text{as} \quad |\alpha R| \to \infty \quad , \\ \\ \dfrac{(\alpha R)^2}{2} \log \dfrac{\alpha R}{A} & \text{as} \quad |\alpha R| \to 0 \quad . \end{cases}$$

Whatever assumption is made about spatial or temporal growth, it is clear that ω/α approaches a complex constant in either limit $|\alpha R| \to \infty$ or $|\alpha R| \to 0$, which means that eigenmodes of very long or very short wavelengths tend to be nondispersive. Modes having wavelengths comparable to the jet diameter are highly dispersive.

To appreciate the dynamical role of dispersion, consider a growing eigenmode $u_1^* \exp i(\alpha x - \omega t)$. The jet column is nonlinear, so the fundamental eigenmode drives a first harmonic of the form $u_2^* \exp i(2\alpha x - 2\omega t)$. If the fundamental is highly dispersive, then the harmonic is not an eigenmode, and u_2^* is a constant and relatively small fraction of u_1^*. The ratio u_2^*/u_1^* involves a resonance denominator, however, which falls to zero when 2α and 2ω themselves satisfy the eigenvalue equation. α,ω and $2\alpha,2\omega$ can be simultaneous solutions of the eigenvalue equation only in regimes of αR where the ratio ω/α is constant, two such regimes being the limits $|\alpha R| \to \infty$ and $|\alpha R| \to 0$. Waves of extreme lengths are nondispersive, resonate with their harmonics, and drive them to large amplitudes. Waves of intermediate lengths produce harmonics that are far from being eigenmodes, so the harmonics are weak.

At the next level of interaction, $u_1^* \exp i(\alpha x - \omega t)$ and $u_2^* \exp i(2\alpha x - 2\omega t)$ couple to drive a higher harmonic and also a wave $u_3^* \exp i(\alpha x - \omega t)$ having the form of the fundamental. To account for nonlinear selection, one need only assume that u_3^* subtracts from u_1^*, in other words, that the harmonic reacts back on the fundamental to inhibit its growth. The fundamental able to attain the largest amplitude is then the wave that generates a harmonic least effectively, the wave furthest removed from resonance with its harmonic, *the most highly dispersive wave on the jet column.* It cannot have an extreme length, since extremely long or short waves are almost nondispersive. It must have an intermediate length proportional to the jet diameter, presumably the length $\lambda = 2.38\ D$ of the mode preferred in the experiments.

The foregoing ideas fit the general theory of Stuart (1960) and Watson (1960) for the evolution of nonlinear dispersive waves. If the assumption is retained that the jet is a uniform column surrounded by a vortex sheet, then the radial eigenfunctions are Bessel's functions, and one comes immediately to the core of Stuart and Watson's theory — the derivation of coupled, first-order ordinary differential equations for the fundamental amplitude, the harmonic amplitude, and a property of the mean field, which in this case is the radius of the jet. Work is already under way on the temporal version of the theory, in which the eigenfunction amplitudes and mean radius depend strictly on time. The temporal theory has the advantage of a dispersion relation c(k) in accord with experiment, because the theoretical phase velocity does not vary with wave amplitude. It may be possible to account for the fact of spatial growth by means of an integral formulation (cf. Ko *et al* 1969). In any event, we can reasonably look forward to a theoretical model of axisymmetric vortex trains, with the preferred Strouhal number of 0.30 emerging by calculation.

References

Batchelor, G. K. & Gill, A. E. 1962 J. Fluid Mech. 14, 529.

Becker, H. A. & Massaro, T. A. 1968 J. Fluid Mech. 31, 435.

Bradshaw, P., Ferriss, D. H. & Johnson, R. F. 1964 J. Fluid Mech. 19, 591.

Bradshaw, P. 1966 J. Fluid Mech. 26, 225.

Browand, F. K. 1966 J. Fluid Mech. 26, 281.

Brown, G. B. 1935 Proc. Phys. Soc. 47, 703.

Crow, S. C. 1970 AIAA J. 8, to be published.

Ffowcs Williams, J. E. 1963 Phil. Trans. Roy. Soc. A 255, 469.

Freymuth, P. 1966 J. Fluid Mech. 25, 683.

Hussain, A. K. M. F. & Reynolds, W. C. 1970 J. Fluid Mech. 41, 241.

Kline, S. J., Reynolds, W. C., Schraub, F. A. & Runstadler, P. W. 1967 J. Fluid Mech. 30, 741.

Ko, D. R. S., Kubota, T. & Lees, L. 1970 J. Fluid Mech. 40, 315.

Landahl, M. T. 1967 J. Fluid Mech. 29, 441.

Leconte, J. 1858 Phil. Mag. 15, 235.

Lees, L. & Gold, H. 1966 *Fundamental Phenomena in Hypersonic Flow.* Proceedings of the International Symposium Sponsored by Cornell Aeronautical Laboratory, Buffalo, 1964. Cornell University Press.

Lumley, J. L. 1966 *Atmospheric Turbulence and Radio Wave Propagation.* Proceedings of the International Colloquium, Moscow, 1965.

Malkus, W. 1956 J. Fluid Mech. 1, 521.

Michalke, A. 1964 J. Fluid Mech. 19, 543.

Michalke, A. 1965 J. Fluid Mech. 23, 521.

Michalke, A. & Wille, R. 1966 *Applied Mechanics.* Proceedings of the Eleventh International Congress of Applied Mechanics, Munich, 1964. New York: Springer.

Moffatt, H. K. 1969 *Computation of Turbulent Boundary Layers.* Proceedings of the AFOSR-IFP-Stanford Conference, Stanford University, 1968. Distributed by the Thermosciences Division, Department of Mechanical Engineering, Stanford University.

Mollo-Christensen, E., Kolpin, M. A. & Martuccelli, J. R. 1964 J. Fluid Mech. 18, 285.

Mollo-Christensen, E. 1967 J. Appl. Mech. 89, 1.

Orszag, S. A. & Crow, S. C. 1970 Studies in Appl. Math. 49, to be published.

Pao, Y.-H., Hansen, S. D. & MacGregor, G. R. 1969 Boeing Scientific Research Laboratories Document D1-82-0863.

Rayleigh, Lord 1896 *The Theory of Sound.* London: Macmillan. Reproduced by Dover Publications.

Reynolds, A. J. 1962 J. Fluid Mech. 14, 552.

Reynolds, O. 1894 Phil. Trans. Roy. Soc. A 186, 123.

Roshko, A. 1961 J. Fluid Mech. 10, 345.

Sami, S., Carmody, T. & Rouse, H. 1967 J. Fluid Mech. 27, 231.

Sato, H. 1960 J. Fluid Mech. 7, 53.

Stuart, J. T. 1960 J. Fluid Mech. 9, 353.

Tyndall, J. 1867 *Sound.* London: Longmans.

Watson, J. 1960 J. Fluid Mech. 9, 371.

Wille, R. 1952 Jahrbuch Schiffbautechn. Ges. 46, 174.

Wygnanski, I. 1964 Aero. Q. 15, 373.

Wygnanski, I. & Fiedler, H. 1969 J. Fluid Mech. 38, 577.